CHARACTERIZATION OF A NANOCOMPOSITE COATING FOR PV APPLICATIONS

CHARACTERIZATION OF A NANOCOMPOSITE COATING FOR SOLAR PANEL APPLICATIONS

By

VICTORIA JARVIS, B.SC.,

A Thesis
Submitted to the School of Graduate Studies
in Partial Fulfillment of the Requirements for the Degree
Master of Applied Science

McMaster University

McMaster University MASTER OF APPLIED SCIENCE (2013) Hamilton, Ontario (Department of Engineering Physics)

TITLE: Characterization of a Nanocomposite Coating for Solar Panel Applications

AUTHOR: Victoria Jarvis, B.Sc. (McMaster University)

SUPERVISOR: Dr. John Preston

NUMBER OF PAGES: vi, 95

Abstract

The development of nanocomposite materials has had significant influence on modern material design. Novel properties can be achieved and controlled for a diverse range of applications. The work presented here focused on the characterization of polyurethane based coatings with ITO nano-inclusions. The coatings displayed high transparency in the visible range, and UV/IR shielding properties when studied with UV-Vis spectroscopy. UV/IR shielding improved with greater ITO density, with minor affect on visible transmittance. The effective medium approximation was successfully applied to ellipsometry data. Coatings with varying fractions of nanoparticles were analyzed. The modeled volume percent of the nanoparticles followed a strong linear trend with the known weight percentages. SEM and TEM imaging determined that majority of the particles existed in clusters. The nanoparticles were oblong shaped, 10-20nm big, randomly distributed, with no segregation to interfaces. Agglomerates varied in size, with the largest observed agglomerate being 250nm.

Thermal stability measurements were carried out by TGA and DSC. No degradation occurred until 238℃. DSC revealed that the matrix continued to go through modifications with consecutive runs. It was inconclusive whether the changes were from the polyurethane or from the dispersive agents in the system. Electron micrographs showed that segregation did not occur after annealing. Average surface roughness increased from 3.5nm to 5nm after annealing at 120℃ for several weeks. Ellipsometry results showed that film thickness decreased 20nm and 50nm before reaching equilibrium for the 80℃ and 120°C anneal respectively. In general, the films displayed good thermal stability up to 120℃. The optical and thermal measurements demonstrated that the coating has great potential for improving the performance of solar modules.

Acknowledgements

I would like to thank my supervisors, Dr. John Preston and Dr. Peter Mascher for giving me the opportunity to work on this endeavor. They were very approachable and supportive, and I was very fortunate to have their expertise through the course of the project. I owe a big thank you to Jessica Carvalho for introducing me to most of the techniques and instrumentation used, and for all our stimulating scientific discussions. I would like to thank Jacek Wojcik for introducing me to the VASE technique, and Frank Gibbs for his work and guidance with DSC and TGA.

I would like to acknowledge the funding provided by the NSERC Photovoltaic Innovation Network, the CREATE program, and CIPI. Also, HyPower for collaborating on this project and supplying the samples.

Finally, thank you to my family for their endless support and encouragement, and my group members and the friends I made in the engineering physics department. You have made these years unforgettable.

Table of Contents

Chapter 1: Introduction

1.1 Nanotechnology

The concept of taking miniaturization to nano-scale dimensions was introduced by the popular lecture “There’s Plenty of Room at the Bottom” by Richard Feynman in 1959. The lecture discussed the possibility of manipulating single atoms, creating nanorobots, and the prospect of storing the entire Encyclopedia Britannica on the head of a pin. Ever since, the mention of nanotechnology became popular in literature, TV, and film. In April 1990, IBM successfully arranged single xenon atoms with a scanning tunneling microscope tip to spell “IBM” on a nickel substrate. Another significant milestone occurred when The Journal of Nanotechnology published its first volume in the year 1990. Interest in the field has since experienced rapid growth due to the vast application potential.

Nanotechnology is a broad area of research aiming to revolutionize materials and their functions. Fields of applications include molecular physics, chemistry, biology, materials, electrical engineering, computer science, and mechanical engineering. The research involves imaging, measurement, modeling, and manipulation of matter at length scales within an approximate range of 1 to 100 nanometers [1]. Nano-sized features are created from either top-down or bottom-up approaches. The former is the creation of nano materials from the successive breakdown of the starting bulk materials. Often, this entails less control at the atomic or molecular level, and the resulting system may contain structural imperfections. The bottom-up technique assembles complex structures from atomic or molecular building blocks allowing for greater control on the properties of the resulting material.

At very small sizes, new physical phenomena arise. Properties of the nano-size material will vary from its bulk counterpart. For example, chemical reactivity for nanoparticles will increase due to greater surface interactions. As the radius of a spherical particle approaches the nanometer scale, the surface-to-volume ratio increases since it holds an inverse relationship.

$$\frac{\textbf{Surface Area}}{\textbf{Volume}} = \frac{4\pi r^2}{\frac{4}{3}\pi r^3} = \frac{3}{r} \qquad [1]$$

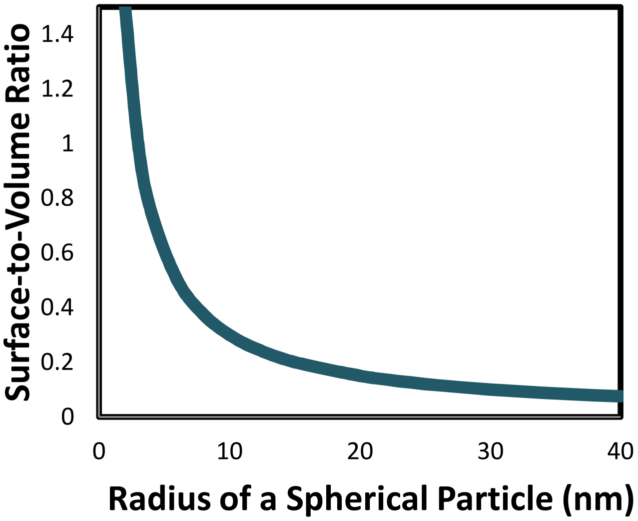

Figure 1.1: The strong dependence of the surface-to-volume ratio on the particle size for small spherical particles.

A high surface-to-volume ratio indicates a larger fraction of atoms are located at the surface and exposed to the surrounding environment. In addition to being physically more accessible, these atoms are more chemically active in comparison to the bulk atoms. Surface atoms have fewer coordinated atoms leading to dangling bonds and sites which will more readily react. This brings forth applications such as contaminant removal in the environment. Iron nanoparticles can readily oxidize in the presence of organic toxins, breaking the toxins down into less harmful compounds [2]. By increasing the number of reactive sites on the surface, interaction with toxic contaminants increases, and the harmful substances are reduced more effectively.

Optical properties of nano materials have also shown new behavior not observed at the micro scale. When light interacts with metallic nanoparticles, it can result in the collective oscillation of the free electrons. This effect is referred to as the surface plasmon resonance (SPR). The dipole polarization which occurs is dependent on the host medium containing the nanoparticles, and will experience a peak resonance when $\varepsilon_{nanoparticles}=-2\varepsilon_{medium}$ for spherical particles, where $\varepsilon_{nanoparticles}$ and ε_{medium} are the dielectric values for the nanoparticles and surrounding medium respectively. A large local field enhancement results at the surfaces of the nanoparticles, increasing light absorption and scattering. For gold, silver, and copper nanoparticles, the SPR frequency is found to lie in the visible wavelength range, giving rise to their bright colours otherwise not observed when in their bulk form. Other factors affecting the SPR frequency include the size and shape of nanoparticles, and the presence of inter-nanoparticle coupling interactions. Consequently, manipulating the physical characteristics and distribution of nanoparticles allows for tunable material behavior for a multitude of applications, such as optical detection of biological and chemical species [3].

Melting temperatures have also been shown to vary with particle size [4], [5], [6]. In bulk materials, the melting temperature is generally independent of size. However, when particle sizes approach the nanometer range, typically a variation of 10-100K in the melting point may be observed. Generally, a depression in the melting temperature occurs due to the increased surface-to-volume fraction of small particles. The high energy surface will more readily melt in order to achieve a lower energy liquid state. Therefore, the smaller the nanopowder is, the greater the influence the surface energy has on the melting temperature. Melting of CdS nanopowders with different particle sizes has shown a decrease close to 600K from the bulk melting temperature [6].

A few challenges in producing nanomaterials include control of size, shape, and degree of aggregation of the material. Significant progress has been made in growth techniques which can achieve desirable characteristics. For developing nanopowders, methods generally fall under gas-phase or liquid-phase synthesis. Flame hydrolysis, chemical vapor condensation, gas condensation, laser ablation or pyrolysis all use gas-phase synthesis. Processes involving liquid-phase synthesis include co-precipitation, micro-emulsion, sol-gel processing, hydrothermal or solvothermal processing, and template synthesis. Often, the particles are functionalized to reduce aggregation, and to improve the miscibility of the nanoparticles to the surrounding medium [7], [8] .

In order to take advantage of the unique tunable characteristics found in nanoparticles, the nanoparticles generally need to be integrated into a structure, or host material. The resulting nanocomposite will have enhanced properties which will be sensitive to the type of host chosen, in addition to the characteristics of the inclusive component. The interest in the research and development of nanocomposites stems from the large application potential. Transparent nanocomposites can be used as protective coatings, or optical lenses due to their durability and broad range of available refractive indices. To characterize the optical behavior of these materials, effective medium theories are often applied.

1.2 Nanocomposites and the Effective Medium Approximation

The ability to predict the response of a material to electromagnetic radiation is essential for many applications. This can only be achieved when the mechanisms responsible for the behavior are well understood. The perceived colour of a material is one indicator of the absorption and reflection behavior of the system. When travelling through one medium into another, light will be absorbed, transmitted, or reflected at the interface. The elemental constituents and structure of the materials will dictate the degree as to which these responses occur. Knowing the index of refraction for both components at the interface, the angle of incidence, and wavelength of light, the optical behaviour can be determined using standard optical theory. However, if light passes through composite materials, the interaction is much more complex.

Optical characterization of nanocomposite materials requires a more involved analysis than for uniform systems, but is much more tractable than for macrocomposites. This is due to the fact that when the nano-sized components are much smaller than the wavelength of light, the light will not scatter because of the presence of two different materials, but will instead, travel through the medium having properties of a certain combination of the individual components. Defining the material as an effective uniform medium is a practical approach to describing its optical behaviour. An effective medium approximation (EMA) models the dielectric response of composite systems based on the characteristics of each component in their pure form. It has been found that only a small volume fraction of nanoparticles need to be present in the material to influence its optical properties [9].

Nanomaterials, or nanocomposites, include any materials which have novel properties due to a nano-scale component. The component may be one dimensional (fibres or nanotubes), two dimensional (layers or plates), or zero dimensional (spherical particles). Incorporation of a nanocomponent has been used to improve mechanical, magnetic, electrical, gas permeability, and optical properties [10], [11], [12], [13], [14]. Only small quantities (1-2%) are often required to obtain desired characteristics [9], [15].

Polymer nanocomposites are composed of a polymeric host matrix with nanoparticle inclusions. Functionalizing polymers in this way allows for the integration of properties found in the inclusion material, while maintaining the flexibility and versatility of the polymer. Traditionally, polymer fillers are on the order of microns in size, or consist of aggregates of that length scale. However, for transparent composites, the particle size should not exceed 40nm in size. If aggregation and segregation of the nanoparticles are avoided, the transparency of the polymer can be maintained. In addition, the integrated nanomaterials can induce absorption or scattering of certain energies, which can be tuned for specific applications. Including a nano-scaled component can also create percolating polymer-particle networks, creating mechanical reinforcement [16], [17].

A number of theories and models have been devoted to determining the optical response of metal particles embedded in a transparent dielectric matrix. Mie theory has completely solved the absorption and scattering of light by a single metal particle [18]. The collective properties of many dispersed metal nanoparticles in a composite may be further described by Maxwell-Garnett theory or the Bruggeman effective medium approximation [18]. Assuming spherical particles having negligible dimensions with respect to the light probe, these theories describe particle polarizability as determined by Rayleigh and Lorentz. These theories are widely used, particularly due to their ease of application. However, systems which fall outside the assumptions made in these approaches will exhibit deviations from the calculated response. In particular, characteristics such as particle shape, interparticle distances, and distribution in the composite will all influence the applicability of an effective medium approximation.

Due to local particle fields interacting with one another as particles become closer, the collective response of composites with high particle loading will stray from the expected effective medium theoretical response. To determine the dielectric divergence when approaching the percolation threshold, some models have applied an empirical scaling factor. Another approach is to use the depolarization distribution function. This model works well if only low order polarizations need to be considered, as in the case for lower particle loading. Other more complex models use a cluster approach with the dipole approximation method.

When developing nanocomposite materials, understanding the shape, distribution, and type of materials used is often necessary to optimize the characteristics for certain applications. Techniques such as electron microscopy and atomic force microscopy will provide information on the distribution and shape of the nanoparticles. Spectroscopy and ellipsometry provide considerable insight on the optical properties of the resulting system. By applying these complementary techniques, the effect of nanoparticle density, size, and dispersion on the optical response can be systematically determined. The system can then be optimized for a specific application.

Transparent nanocomposites are of particular interest for technologies including lighting and displays, UV-protective coatings, IR active fillers, lenses, optical filters or reflectors, and antireflection coatings. Generally, the index of refraction of polymers is limited since most polymers fall within the range of 1.3 to 1.7. Polymer nanocomposites expand this range, allowing for low and high refractive materials. The most relevant application for the composite coating described in this document is as a UV and IR shield. Infrared absorbing pigments, such as indium tin oxide (ITO), are researched for heat reflection in windows. UV-absorbing materials can improve the stability of the polymers, as well as shield any underlying material from UV radiation. Solar cells can benefit from such a protective layer since only part of the visible range of light is efficiently converted. By reducing the infrared and ultraviolet regions of the spectrum, the amount of unusable or excess light which normally contributes to heating the solar module will decrease. Solar cells operate most efficiently at lower temperatures. Therefore, coating an encapsulated solar module with a transparent polymer composite containing a UV-absorbing pigment can potentially improve the performance and lifetime of a solar module.

1.3 Solar Energy

As the supply of fossil fuels diminishes, and environmental concerns grow, the need for clean and renewable energy is becoming more apparent. Combustion based generators produce large volumes of harmful emissions which are known to have detrimental effects on population health, biological ecosystems, and the climate. In 2008, 72% of sulfur dioxide emission in the

United States came from electrical generation [19]. Sulfur dioxide is an air pollutant which acts as a precursor to acid rain. Acid deposition leads to changes in soil and water quality, and as a result can have significant impact on aquatic life, forests, and vegetation. The implementation of pollution regulations and increases in fuel cost, motivate the progression toward greener technologies.

Currently, hydropower leads the renewable energy sector in the world. Despite the large increase in the use of solar power generation over the past few years, it holds only a small share of the renewable energy pool. In order to become a viable competitor, photovoltaic technology needs improvements in costs and efficiency.

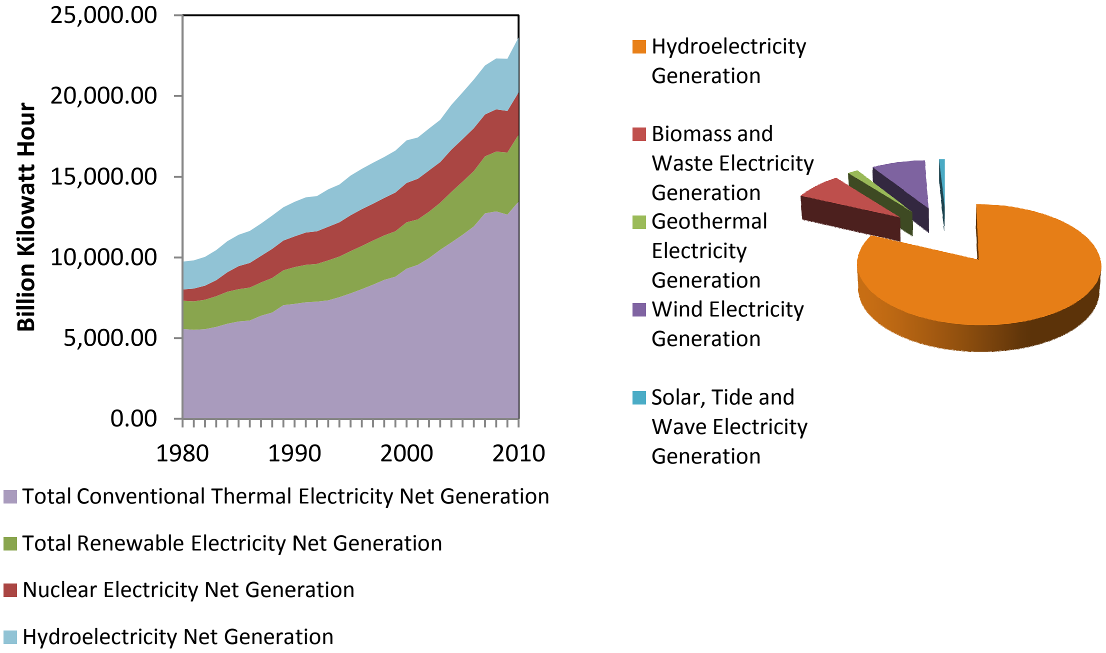

Figure 1.2: (a) Total world net contribution of different forms of electricity generation and (b) renewable sources of electricity and their share in the net renewable energy generation in 2010 obtained from the US Energy Information Administration [20]**.**

Solar cells convert light from the sun into electrical power. When light interacts with the semiconductor which comprises the cell, a certain portion of the solar spectrum will be absorbed. The energy absorbed goes to exciting electrons, allowing the carriers to move freely through the material. In the presence of a potential, the electrons are drawn out for external use as an energy source.

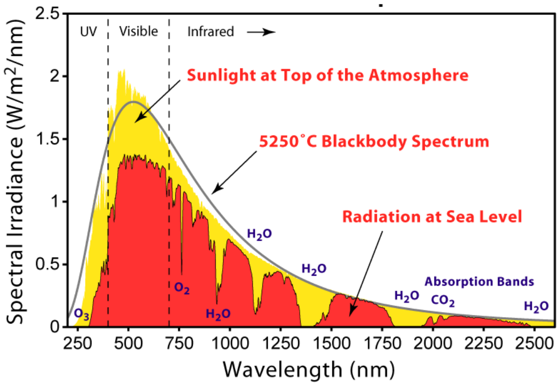

Figure 1.3: The solar spectrum, indicating in red the portion of electromagnetic radiation reaching Earth. Image created by Robert A. Rohde for Global Warming Art [21]**.**

1.4 Thermal Challenges in Solar Cells

As stated at the end of Section 1.2, the efficiency of photovoltaic cells is significantly limited by thermal effects. When a cell is exposed to an optical spectrum, a fraction of the light contributes to increasing the temperature of the solar module instead of producing electrical output. The band gap of the material limits which wavelength of light has enough energy to excite an electron into its conduction band. Photons with energy below the band gap will be absorbed by free carriers, which produce heat as they relax back to the band edge. Any sub-bandgap light which is not absorbed through this process will be converted to heat at the cell's back contact. Conversely, when photons with energy greater than the band gap are absorbed, the electrons have excess energy which is released into the lattice as they thermalize to the edge of the conduction band. The energy absorbed by the lattice results in lattice vibrations, or heat. Finally, any radiation not absorbed in the active region of the device will typically reach the metalized back contact, where it will be absorbed, producing heat.

If considering an open circuit cell exposed to light, then the open circuit voltage, V_{OC}, would be the voltage required for no current to flow. The photogenerated current is opposed by the drift current which results from the V_{OC}. The recombination rate also reduces the photogenerated current and consequently, the V_{OC} required is reduced. The open-circuit voltage, V_{OC}, is the most sensitive parameter to temperature and is determined by the balance between recombination rate and photogeneration rate [22]. The underlying reason for the dependence of solar cell performance on temperature results from increasing carrier recombination rates, and as a result, reduction in minority carrier lifetime. Although the short circuit current, I_{SC}, slightly increases with temperature due to a decrease of the band gap, the V_{OC} decreases significantly, causing the solar cell to output less power. For example, in a SunPower maxeon^{TM} monocrystalline silicon solar cell, the efficiency drops by -0.38% per degree Celsius increase in temperature [23].

When an open circuit cell is illuminated, the excitation of electrons into the conduction band creates a current. This drives the system out of thermal equilibrium, and the steady state Fermi levels on the p and n side of the junction no longer line up. Each side now has its own quasi-Fermi level, and the difference corresponds to the open-circuit voltage. When recombination occurs, a conduction band electron relaxes back to the valence band or mid-gap state which may eventually recombine with a hole. Recombination rate will move against the light induced bias, reducing the difference between quasi Fermi levels. Recombination is directly proportional to temperature. When the light-generated current and recombination current balance one another, a net current of zero occurs. The measured voltage is the open circuit voltage and will therefore vary with temperature as well.

Temperature coefficients are one way to classify the temperature dependence of photovoltaic performance. The values are often presented as the change in short-circuit current or open-circuit voltage. The temperature dependence is given by

$$\boldsymbol{I_{sc}(T) = I_{sc}(25^{\circ}\mathrm{C})[1 + \alpha_{SC}(T - 25^{\circ}\mathrm{C})]\frac{Irradiance}{1000\frac{W}{m^2}}} \quad [1]$$

$$\boldsymbol{V_{oc}(T) = V_{oc}(25^{\circ}\mathrm{C})[1 + \beta_{OC}(T - 25^{\circ}\mathrm{C})]} \quad [2]$$

where α_{SC} and β_{OC} are the short-circuit current and open-circuit voltage coefficients respectively [24]. In general, temperature coefficients for mono- or polycrystalline cells are higher than those found for thin film technology.

1.5 Solar Cell Nanocomposite Coatings

One approach to managing the heat problem is through the use of a transparent coating which is capable of blocking high UV and IR radiation. Taking advantage of the transparency and durability of polymers, and combining it with a heavily doped, wide band gap semiconductor material, a composite coating with high visible wavelength transparency and UV/IR shielding can be created. In order to optimize visible wavelength transparency, the semiconductor component needs to be incorporated into the polymer matrix as nanoparticles to reduce losses by Rayleigh scattering. The dielectric function, size, volume fraction, and distribution of the nanoparticles will tune the optical properties of the composite [25]. These variables can be optimized for solar cell applications.

A difficulty encountered in manufacturing nanocomposites is achieving an appropriate dispersion of the nanoparticles in the host material. For nanocomposites requiring high transparency, agglomeration and aggregation needs to be minimized. Traditional methods for synthesizing solid powders, such as pyrolysis or precipitation, tend to form chemically bonded aggregates during the process. Therefore the particles need to be created independently, such that they do not chemically interact. The usage of additives or dispersive agents is common. A second important consideration is the compatibility of the materials. Incorporating hydrophilic particles into a hydrophobic organic polymer creates an unstable system causing nanoparticles to aggregate. To integrate particles successfully, the particle surface can be functionalized with the intention of increasing the miscibility of the particles in the polymer.

Alone, polymers are ineffective at shielding ultraviolet light. With the addition of wide-band gap particles, a UV-shielding coating with high visible transparency can be obtained. Polymer systems containing TiO_2, ZnO, and CeO_2 have demonstrated high UV absorption with low particle concentration [26]. Indium tin oxide (ITO) has been reported as having high reflectivity in the infrared region, great thermal stability, as well as absorption in the UV range [27].

1.6 Research Motivation

The research presented in this document involves the characterization of a coating with potential UV/Vis shielding properties for solar cell applications. Using nanocomposite technology, the coating is expected to display high transparency in the visible range, but controlled shielding in the near-IR to ultraviolet range. If applied to solar modules, reducing the amount of unusable light interacting with the solar cell will keep the operating temperature of the solar cell lower, reducing efficiency losses. To determine the suitability of the coating material in field applications, this research focuses on the optical, physical, and thermal characteristics of the nanocomposite coating.

Chapter 2: Background

2.1 Optics of Solids: Theoretical Formulation

When light propagates through solid media, various optical phenomena can be observed. Selective absorption, dispersion, birefringence, and polarization effects are just a few examples. Most of the optical behavior of solids can be understood through classical electromagnetic theory, starting with Maxwell's macroscopic equations. These equations provide physical insight into numerous optical systems, and are a suitable starting point for understanding a material's optical response.

At a particular point in space, four quantities can be used to describe the electromagnetic state of matter: electric charge density (**ρ_Q**), electric dipole density known as the polarization (**P**), magnetic dipole density known as magnetization (**M**), and the current density (**J**). These quantities, forming the Maxwell's equations, define the electric and magnetic field **E** and **H**, and can be written as

$$\nabla \times \boldsymbol{E} = -\mu_0 \frac{\partial H}{\partial t} - \mu_0 \frac{\partial M}{\partial t} \qquad [3]$$

$$\nabla \times \boldsymbol{H} = \epsilon_0 \frac{\partial E}{\partial t} + \frac{\partial P}{\partial t} + \boldsymbol{J} \qquad [4]$$

$$\nabla \cdot \boldsymbol{E} = -\frac{1}{\epsilon_0} \nabla \cdot \boldsymbol{P} + \frac{\rho_Q}{\epsilon_0} \qquad [5]$$

$$\nabla \cdot \boldsymbol{H} = -\nabla \cdot \boldsymbol{M} \qquad [6]$$

The polarization, **P**, quantifies the collective response of the bound charges when an electric field is applied. The proportionality factor relating **P** to **E** is referred to as the electric susceptibility, χ, shown as

$$\boldsymbol{P} = \chi \epsilon_0 \boldsymbol{E} \qquad [7]$$

In the optics of solids, χ is an important parameter which effectively describes the degree of polarization. For isotropic media, the electric response is the same for all directions of the applied electric field, and therefore χ is described as a scalar.

For media which is anisotropic, χ is a tensor which can effectively summarize most of a crystal's optical properties. A general wave equation derived from the above Maxwell's equations is

$$\boldsymbol{\nabla} \times (\boldsymbol{\nabla} \times \boldsymbol{E}) + \frac{1}{c^2}\frac{\partial^2 E}{\partial t^2} = -\mu_0 \frac{\partial^2 P}{\partial t^2} - \mu_0 \frac{\partial J}{\partial t} \qquad [8]$$

The two terms on the right side of the general equation describe the presence of polarization and conduction charges. For non-conducting media, the polarization term is important in explaining optical phenomena in a material. To explain the opacity and high reflectance of metals, the conduction term provides the most insight. For semiconductor materials, it is necessary that both terms are considered.

In isotropic, non-magnetic, and electrically neutral media, the solution to the general wave equation results in a polarized transverse wave propagating at a phase velocity of c/*n*, where *n* is the index of refraction of the medium in which the wave is travelling. If the positive z-direction in a Cartesian coordinate system is defined as the propagation direction, the electric field is

$$E(z,t) = E_0 e^{-\alpha z} e^{i(kz-\omega t)} \qquad [9]$$

where $e^{-\alpha z}$ represents an exponential decrease in the amplitude of the wave as it is being absorbed by a material. The complex index of refraction and extinction coefficient are

$$\mathrm{N} = \mathrm{n} + i\kappa \qquad [10]$$

$$\mathrm{N}^2 = \varepsilon = \varepsilon_1 + i\varepsilon_2 \qquad [11]$$

The square of the index of refraction can be expanded and separated into the real and imaginary components, defining ε_1 and ε_2

$$\mathrm{N}^2 = \mathrm{n}^2 - \kappa^2 + i2\mathrm{n}\kappa \qquad [12]$$

$$\varepsilon_1 = \mathrm{n}^2 - \kappa^2 \qquad [13]$$

$$\varepsilon_2 = 2\mathrm{n}\kappa \qquad [14]$$

The electromagnetic absorption of a medium, α, can be determined from the imaginary component of the complex index of refraction using

$$\boldsymbol{\alpha = \frac{4\pi}{\lambda}} \qquad [15]$$

Up to now, the behavior of light as it travels through a medium has been discussed. However, to understand a reflection or transmission experiment, the interaction of light at a dielectric boundary needs to be addressed. Due to a change in velocity the light experiences, the propagation direction also varies. This phenomenon is described by Snell's law of refraction

$$\boldsymbol{n_1 \sin\theta_1 = n_2 \sin\theta_2} \qquad [16]$$

When light travelling at oblique incidences is transmitted or reflected off a sample, the p and s components behave differently. Each component consists of an electric field **E** and a magnetic induction **B** vector. The boundary conditions for electromagnetic waves state that vectors parallel to a boundary are continuous, equal on incident side and transmission side. For p polarized light

$$\boldsymbol{E_{ip}\cos\theta_i - E_{rp}\cos\theta_r = E_{tp}\cos\theta_t} \qquad [17]$$

$$\boldsymbol{B_{ip} + B_{rp} = B_{tp}} \qquad [18]$$

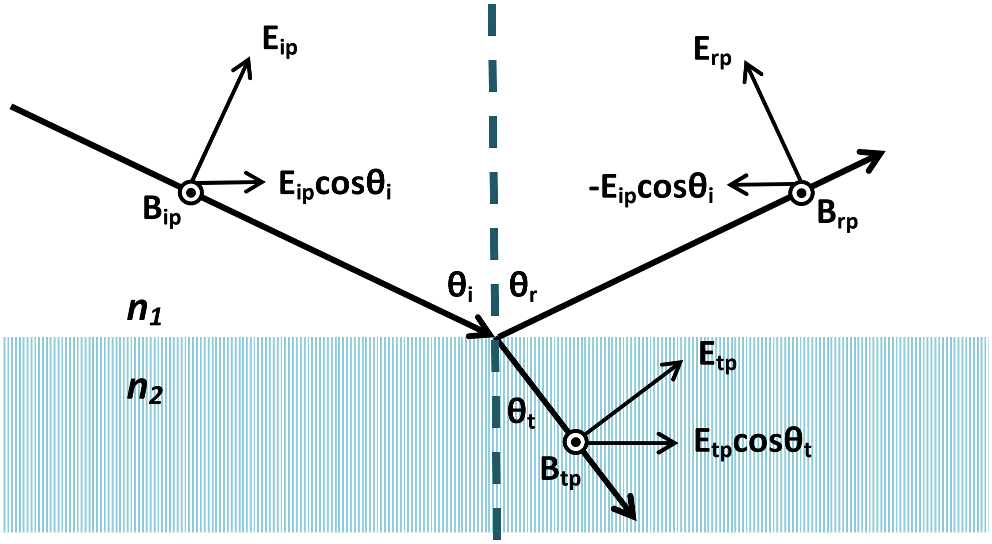

Figure 2.1 Interaction of p polarized light at a boundary. The electric field and magnetic induction vectors satisfy the boundary condition. (Adapted from [28]**)**

Since **E**=c**B**, a medium with an index of refraction of n can have its magnetic component rewritten as

$$\mathrm{n_i}\left(E_{ip} + E_{rp}\right) = \mathrm{n}_t E_{tp} \qquad [19]$$

Substitution into the boundary condition equation for $\mathbf{E}_{tp}$ or $\mathbf{E}_{rp}$, the Fresnel amplitude coefficients for reflected or transmitted light can be defined respectively

$$r_p \equiv \frac{E_{rp}}{E_{ip}} = \frac{n_t \cos\theta_i - n_i \cos\theta_t}{n_t \cos\theta_i + n_i \cos\theta_t} \qquad [20]$$

$$t_p \equiv \frac{E_{tp}}{E_{ip}} = \frac{2n_i \cos\theta_i}{n_t \cos\theta_i + n_i \cos\theta_t} \qquad [21]$$

In a similar manner, the Fresnel amplitude coefficients can be derived for s-polarized light

$$r_s \equiv \frac{E_{rs}}{E_{is}} = \frac{n_i \cos\theta_i - n_t \cos\theta_t}{n_i \cos\theta_i + n_t \cos\theta_t} \qquad [22]$$

$$t_s \equiv \frac{E_{ts}}{E_{is}} = \frac{2n_i \cos\theta_i}{n_i \cos\theta_i + n_t \cos\theta_t} \qquad [23]$$

For materials with a complex index of refraction, the above equations still hold true if n is substituted by N. The amplitude coefficients can then be represented in the polar coordinate system

$$\boldsymbol{r_p = |r_p| exp(i\delta_{rp})} \quad [24] \qquad \boldsymbol{r_s = |r_s| exp(i\delta_{rs})} \quad [25]$$

$$\boldsymbol{t_p = |t_p| exp(i\delta_{tp})} \quad [26] \qquad \boldsymbol{t_s = |t_s| exp(i\delta_{ts})} \quad [27]$$

To quantify the reflection process, the ratio of the complex amplitude coefficients is used, denoted by ρ_r

$$\boldsymbol{\rho_r = \frac{r_p}{r_s} = \frac{|r_p|}{|r_s|} exp[i(\delta_p - \delta_s)]} \quad [28]$$

Substituting tanΨ as the relative amplitude ratio and Δ for the phase shift difference between the p and s components, the fundamental equation of ellipsometry which relates the measured parameters Δ and Ψ can now be written

$$\boldsymbol{\rho_r = \tan\Psi\, exp(i\Delta)} \quad [29]$$

Knowledge of the behavior of light at a boundary is a building block to an understanding of the total reflection of a multilayered system. Light travelling through a multilayered material will have a complex system of reflecting and transmitting waves at each interface. These waves overlap, resulting in optical interference. The interference effect is used in ellipsometry to determine layer thicknesses.

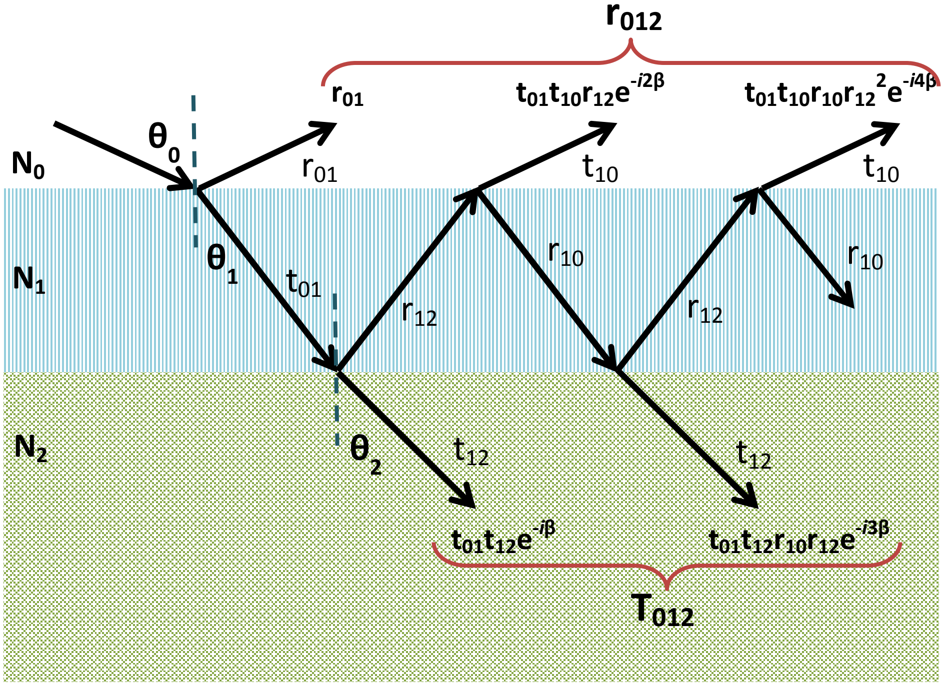

Figure 2.2: Optical interference of light through an ambient-thin film-substrate system. Transmission and reflection amplitude coefficients, r_{jk} and t_{jk}, are labeled for each interface interaction. N_i refers to the complex refractive index for the *i*th layer. The terms r_{ij} and t_{ij} are the amplitude reflection and transmission coefficients after the light interacts with the ij interface. (Adapted from [28])

If absorption of the thin film is low, then reflection off the surface will consist of the primary reflected beam overlapping with multiple other beams reflected from the underlying interfaces. The amplitude of the reflected light will depend on the difference in phase of the interacting beams. To represent the phase difference between the interface and the surface, a variable β is used, and defined as α=2β. Each beam coming off an interface can have an amplitude coefficient assigned to it. The sum of all the amplitudes of the reflected waves off the surface gives the amplitude reflection coefficient of the sample system

$$r_{012} = r_{01} + t_{01}t_{10}r_{12}e^{-i2\beta} + t_{01}t_{10}r_{10}r^{2}{}_{12}e^{-i4\beta} + t_{01}t_{10}r^{2}{}_{10}r^{3}{}_{12}e^{-i6\beta} + \cdots \qquad \textbf{[30]}$$

An infinite series where y=a+ar+ar^2+ar^3+… simplifies to y=a/(1-r). Applying this function to the equation above gives rise to

$$\boldsymbol{r_{012}} = \frac{\boldsymbol{r_{01}+r_{12}\mathbf{exp}\,(-i2\beta)}}{\boldsymbol{1+r_{01}r_{12}\mathbf{exp}\,(-2\beta)}} \qquad [\mathbf{31}]$$

Similarly, the amplitude transmission coefficient is

$$\boldsymbol{t_{012}} = \frac{\boldsymbol{t_0t_{12}\mathbf{exp}\,(-i\beta)}}{\boldsymbol{1+r_{01}r_{12}\mathbf{exp}\,(-i2\beta)}} \qquad [\mathbf{32}]$$

To describe the polarization state of light, it is convenient to use two orthogonal, linearly polarized states as the basic components. Then, the difference in the phase of the fields and the propagation direction are the only terms necessary to describe the state of polarization. A shift in phase between the orthogonal components will result in light which is linearly, circularly, or elliptically polarized, depending on the extent of the shift. An electromagnetic wave travelling in the z-direction can be resolved as a vector sum of electric fields **E**$_x$ and **E**$_y$

$$\begin{aligned}\boldsymbol{E(z,t)} &= \boldsymbol{E_x(z,t) + E_y(z,t)}\\ &= \boldsymbol{\{E_{x0}exp[i(\omega t - Kz + \delta_x)]\}x + \{E_{y0}exp[i(\omega t - Kz + \delta_y)]\}y}\end{aligned} \qquad [\mathbf{33}]$$

where **x** and **y** are unit vectors along the corresponding coordinate axes. In describing the polarization state, absolute values are not essential; rather, the relative difference in phase is important. This is true for measurements in ellipsometry. If the phase difference is zero between **E$_x$** and **E$_y$**, the light is linearly polarized. A shift of 90° (δ_y - δ_x = π/2) causes the resulting vector to rotate in the xy plane as the light propagates, referred to as circularly polarized. When the phase shift is π/4, the light is elliptically polarized.

2.2 The VASE Measurement

To obtain the ellipsometry values Ψ and Δ, the sample is irradiated with p- and s- polarized light. As light transmits or reflects at sample boundaries, the polarization state changes. Based on the change, optical constants and film thickness can be determined. In ellipsometry, the polarization state of incident and reflected light are defined by the coordinates of p- and s- polarization. Upon reflection, p- and s- show different polarization characteristics

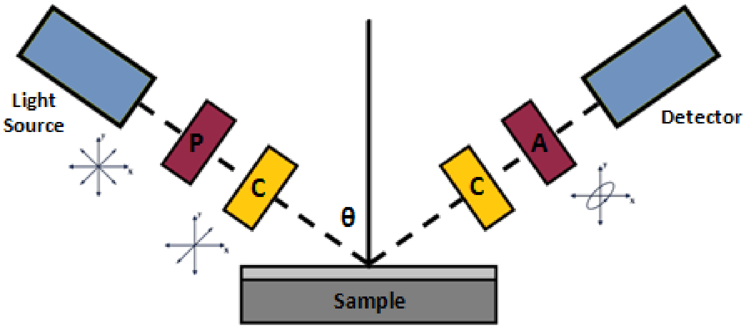

Figure 2.3 The principle of the ellipsometry measurement (Adapted from [28]**). Light emitted from the source will pass through a polarizer. If a compensator is present, it may be located before or after interaction with the sample. Finally, the light polarized by the sample will travel through an analyzer prior to entering the detector. The change in polarization state induced by the interaction with the sample is determined from the measured intensity and orientation of the polarizer, analyzer, and compensator if present.**

2.2.1 Optical Elements

To experimentally determine the polarization state of light, several optical components are required. In ellipsometry there are three types of optical components; polarizers, compensators, and depolarizers. Polarizers filter unpolarized light resulting in linearly polarized light. An optical compensator, also known as a retarder, is able to introduce a specific phase between the two basis states so that it can for instance convert linearly polarized light to circularly polarized light. The depolarizer is used when polarized light is converted to unpolarized light. This section will go over each of these optical components in more detail, as well as their role in the ellipsometry measurement.

In an ellipsometer, there are two polarizers present, each serving a different role in the measurement. The first polarizer is situated in front of the light source and converts the outgoing unpolarized light into linearly polarized light. The second polarizer, referred to as the analyzer, is located in front of the light detector. The polarization state of the reflected light beam is determined from the transmitted intensity out of the analyzer. Both the polarizer and analyzer are made of the same optical component, but are utilized in different ways.

A polarizer is often made up of a calcite crystal. The calcite structure is comprised of alternating layers of calcium and electron rich carbonate. When a material interacts with light in the UV/visible range, the refractive index is governed by the electric polarization. The carbonate planes in the structure will more easily undergo dielectric polarization due to the higher concentration of electrons, and will therefore have a higher index of refraction than in the direction perpendicular to the layers. Materials showing a directional dependence of index of refraction are described as having optical anisotropy. The electric field parallel to and perpendicular to the structure's Ca and CO_3 layers are defined as E_o and E_e, or ordinary and extraordinary rays respectively. Recalling that the velocity of a propagating wave is c/n, and that $n_o > n_e$ in calcite, it is apparent that the extraordinary ray travels faster than the ordinary ray. At oblique angles of incidence, the two rays experience different electronic environments and will propagate at different angles through the medium. It is this behavior which allows for the isolation of linearly polarized light from an unpolarized light source.

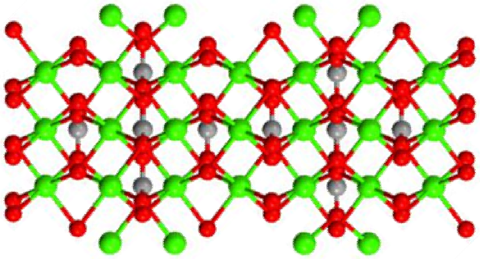

Figure 2.4: The calcite structure [29]**. Planes of calcium atoms in green are layered between planes of electron rich carbonate groups. Carbon is shown in grey and oxygen in red.**

The actual structure of the polarizer consists of two prisms. To only transmit light travelling in a single direction, total reflection is used. The light propagating through the calcite crystal eventually meets the prism/air interface between the two prisms. The prism is cut such that the angle at which the light approaches the interface, is the critical angle for total reflection,

$$\sin \boldsymbol{\theta}_c = \frac{\mathbf{1}}{\boldsymbol{n}_i} \qquad \textbf{[34]}$$

By adjusting the incident angle to the critical angle, the ordinary ray is removed by total reflection and only the extraordinary ray transmits through. The second prism then takes the transmitted light and redirects it so that it is parallel with the incident beam. This type of polarizer is referred to as a Glan-Taylor or Glan-Thompson prism, depending if the optical axes of the prisms are both parallel or perpendicular to the reflection plane. A third type of polarizer, a Rochon prism, uses two prisms with optical axes perpendicular to one another, allowing for rotation of the element.

To convert linearly polarized light into circularly polarized light, or vice versa, a compensator can be utilized. Like a polarizer, a compensator uses a birefringent crystal. The light propagating through the crystal will have one electric field component parallel to the slow axis and the other perpendicular to the fast axis of the crystal. A difference in phase results and the final polarization state of the transmitted light can be controlled by the thickness of the compensator crystal. The phase difference relationship is

$$\boldsymbol{\delta = \frac{2\pi}{\lambda}|n_e - n_o|d} \qquad \textbf{[35]}$$

with *d* denoting the thickness of the crystal, and n_e and n_o corresponding to the extraordinary and ordinary axes respectively [30]. The compensator is often referred to as a quarter-wave plate because it is designed to create a phase difference of λ/4, leading to circularly polarized light. Due to its high transmittance in the UV region, MgF_2 is now widely used. The difference in n_e and n_o in calcite is quite high, and in order to achieve circularly polarized light a very thin crystal is required. A compensator made of MgF_2 allows for a thicker and more robust crystal for ellipsometry, and is therefore preferred over calcite.

Another component often found in spectroscopic ellipsometers is the depolarizer. The light source used for the measurement predominantly produces unpolarized light. However, there are some components in the emitted light which have slight polarization. This effect is referred to as the source polarization. Detectors have shown to vary in sensitivity towards different polarizations of light [31]. To eliminate source polarization and the discrepancy in the sensitivity of the detector, a depolarizer is placed in front of the detector.

2.2.2 Data Modeling

When analyzing spectroscopic ellipsometry data, the dielectric functions of the system are needed. If unknown, the dielectric function needs to be modeled. Depending on the type of material, it is important to select a suitable model to describe its optical properties. In spectral regions where the material is transparent, the Sellmeier [32] or Cauchy model [28] is applied. Free-carrier absorption is often modeled using the Drude model [28]. Many models exist for modeling the optical behavior when electric polarization occurs in the UV-Vis spectral region. A few examples of these models include the Lorentz, Tauc-

Lorentz, and the harmonic oscillator approximation. For systems showing more complicated behavior, different models may be used to characterize different regions of the spectrum.

Due to their high transparency, polymers are generally characterized using the Cauchy model. Applying ε_2=0, the Cauchy model is derived and simplified from the Lorentz model. The Cauchy model is expressed by

$$\mathbf{n} = \mathbf{A} + \frac{\mathbf{B}}{\lambda^2} + \frac{\mathbf{C}}{\lambda^4} + \ \ldots \qquad \textbf{[36]}$$

which is essentially a series expansion of the Sellmeier equation. The analytical parameters A, B, and C are determined in the data analysis and define the shape of the dielectric dispersion. Some semiconductor materials can also be partially characterized using the Cauchy model for energies of light below the bandgap, if κ=0. Modelling wide bandgap materials such as tin-doped indium oxide can be broken down into 2 or more parts. In the visible spectral region, ITO is transparent and the Cauchy model will represent the dielectric function. In the IR and UV regions, a function such as the Lorentz oscillator needs to be applied.

When electric polarization occurs, the Lorentz model assumes that an electron oscillates as if it were bound to its atomic nucleus by a spring. The electron in this case is assumed to oscillate in a viscous fluid, and the balance of forces associated with the motion yields

$$\boldsymbol{m_e} \frac{\mathbf{d}^2 \boldsymbol{x}}{\mathbf{d}\boldsymbol{t}^2} = -\boldsymbol{m_e \Gamma} \frac{\mathbf{d}\boldsymbol{x}}{\mathbf{d}\boldsymbol{t}} - \boldsymbol{m_e \omega_o^2 x} - \boldsymbol{e}\mathbf{E}_{\boldsymbol{o}} \mathbf{exp}\ (\boldsymbol{i\omega t}) \qquad \textbf{[37]}$$

with m_e and *e* corresponding to the electron mass and charge respectively. The first term on the right side is the viscous force of the fluid where Γ is the dampening coefficient. The second term describes the movement of the electron due to the applied electric field, following Hook's law and oscillating with a resonant frequency of ω_0. The final term in the equation refers to the electrostatic force. The oscillation that results from the applied ac field will have the same frequency as the applied ac field. The solution to the equation can assume the form x(t) = *a* exp(*i*ω*t*), and substituting the appropriate derivatives and applying the definition of the dielectric constant, Equation 37 becomes

$$\varepsilon = 1 + \frac{e^2 N_e}{\varepsilon_0 m_e} \frac{1}{(\omega_0^2 - \omega^2) + i\Gamma\omega} \qquad \textbf{[38]}$$

where N_e corresponds to the number of electrons per unit volume. In the analysis of ellipsometry data, the Lorentz model is described in terms of the photon energy, and the dielectric function will consist of the sum of all oscillators.

$$\varepsilon = 1 + \sum_j \frac{A_j E n_{0j}}{E n_{0j}^2 - E n^2 - i\Gamma_j E n} \qquad \textbf{[39]}$$

The A_j term describes the oscillator strength of the jth oscillator.

To model the nanocomposite studied, the polymer alone will first be characterized by the Cauchy model. Once the analytical parameters A, B, and C are determined, they will be fixed for the modeling of the nanocomposite. The ITO nanoparticles will also be characterized by a Cauchy model, except in a fixed spectral range where ITO is transparent. The model will then be expanded to the full spectrum and include Lorentz oscillators to describe the polarization events which occur.

2.3 Polyurethanes

Polyurethane (PU) coatings are used for a diverse number of applications. In the automotive industry, PU coatings improve colour retention, and protect against scratching and corrosion. Spray coating of PUs on building floors and concrete supports improves durability and reduces maintenance costs [33]. The interest in polyurethanes, as in many block polymers, stems from the wide selection of monomeric building-blocks available. Different structural components, and combinations of components, will form polymers with properties optimized for their application.

Polyurethane block polymers are comprised of alternating soft and hard segments. The softer segments have lower glass transitions and are made up of polyethers or polyesters. The harder, more rigid segments have glass transitions well above room temperature and are formed from the combination of a diisocyanate and polyol. The bond between the segments is referred to as a urethane linkage. Block copolymers tend to experience domain microstructuring as a consequence of the difference in the chemical nature of the segments. With the segments preferentially grouping together, the polymer chains fold in a way which creates separate regions of soft segments and hard segments.

The chemical composition and size of the soft segment greatly affect the resulting macroscopic properties of the polyurethane. In particular, the chemical structure will influence the miscibility between the soft and hard segments. Increasing the length of the soft segment has shown to increase domain separation [34], [35].However, if functionalized, the soft segment will demonstrate less phase separation and the polyurethane will have greater strength [36].

Hydrogen bonding plays a major role in the polyurethane structure. The urethane –NH group functions as the electron donor. The ether oxygen, the carbonyl from the urethane or the ester functional group will act as the electron acceptor [33]. Since there are a number of combinations of sites for hydrogen bonding, with different bond energies, a system out of equilibrium would be expected to undergo significant modification before it reaches a low energy state. The types, locations, and frequency of these sites will have an effect on the overall structure, and as a result, affect the material's physical properties.

2.4 Spin Coating

Coatings to be tested were prepared by spin casting. Spin casting, also sometimes referred to as spin coating, is widely used in the fabrication of thin film coatings. The technique allows for high reproducibility and structural uniformity, ideal for a variety of applications. It is commonly used for applications such as protective coatings, optical coatings, and application of photoresists [37].

The process involves dropping a solution on a substrate or surface. The solution may be added to a substrate which is initially stationary or rotating with a low angular velocity. The system is then accelerated to a high angular velocity, causing the solvent to eject or evaporate. During rotation, the solution flows radially due to the centrifugal forces acting on it. The schematic is shown in Figure 2.5. A solid uniform film coating remains once the casting is complete.

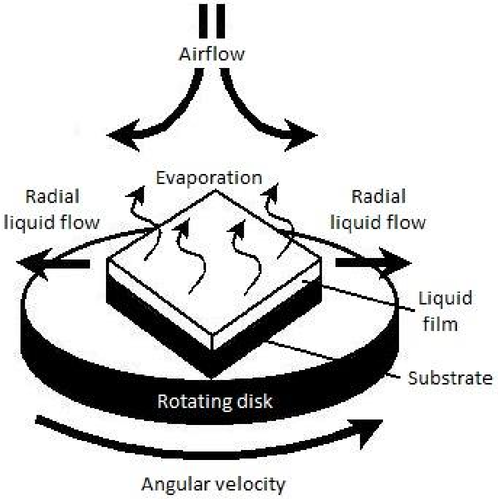

Figure 2.5: A schematic of the spin casting process.

There are many factors which will influence the resulting thickness of the film. The angular velocity and concentration of polymer are strongly correlated with the final film thickness. Other factors include the properties of the polymer and the solvent, as well as all the interactions between polymer, solvent, and substrate. The process can be described by the empirical relationship:

$$\boldsymbol{h = k_1 \omega^{\alpha}} \qquad [40]$$

where h is the thickness of the film, ω is the angular velocity, and k_1 and α are empirical constants. Many authors have found that the α term is approximately -

0.5 [37]. The resulting thickness is directly proportional to the concentration and the relationship is shown in Figure 2.6.

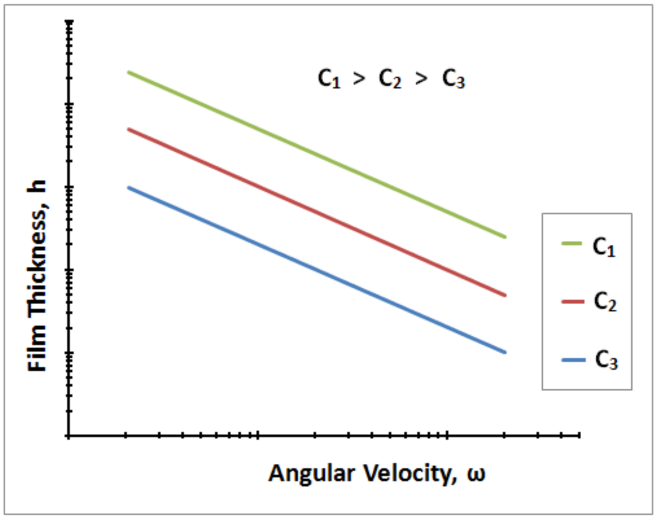

Figure 2.6: The dependence of concentration and film thickness on the angular velocity.

Equation 40 can be expanded to include a term for concentration

$$h = k_2 {\eta_0}^{\beta} \omega^{\alpha} \tag{41}$$

where the exponent β in the viscosity term η_0 is typically within the range of 0.29-0.39 for polymeric solutions. The dependence on the type of polymer/solvent system studied was investigated by Spangler *et al* [38]. The work concluded that the varying interactions between polymer, solvent, and substrate are likely considered in the proportionality constant k_2, not in α or β.

Spin casting was used for the preparation of all the film samples discussed in this work. To obtain a range of thicknesses, the starting solution was diluted with ultra pure deionized water. Varying the ratio of water to polymer allowed for the production of films with a range of thicknesses. Coatings casted on cleaved squares of silicon wafer were used for electron microscopy and ellipsometry measurements. Films cast on glass cover slips were used for transmittance measurements in the UV-Vis spectrophotometer.

Chapter 3: Optical Characterization

Variable angle spectroscopic ellipsometry (VASE) was used to determine the optical behaviour of the coating containing various loadings of ITO nanoparticles. Obtaining the dielectric function of the coating is important for determining the optimal parameters for solar cell applications. The resulting n and **κ** can be used to calculate the ideal coating thickness and loading to maximize the efficiency of the solar module. For example, by manipulating the thickness and loading of the sample, the amount of UV radiation which is blocked can be controlled. Since the open framework design of most solar panels allows for some dissipation of heat from the cells, it may not be necessary to completely block higher energy radiation. The gain in electrical output from partially transmitting higher energy radiation may be greater than the loss in conversion efficiency due to heat. In other words, the coating should be optimized based on a module's typical operating temperature.

Characterization of the nanocomposite layer was accomplished by applying an effective medium approximation (EMA) to the VASE model. Several steps were involved in building up the nanocomposite model to reduce the number of working variables. First, the polyurethane matrix without any embedded nanoparticles was examined in order to fix the dielectric function as the first component in the EMA layer. Next, measurements of the surface roughness of several samples were obtained using atomic force microscopy (AFM) and then fixed in the model. When modeling the dielectric dispersion of ITO and the EMA volume percent of nanoparticles, the data was fixed within the expected transparent range of ITO, where $\kappa=0$. R.A. Synowicki [39] has previously applied this method successfully in modeling ITO thin films, to avoid correlation of variables. Finally, the fit can be applied to the full range of data, fixing the determined EMA% and film thickness. The optical dispersion for each nanoparticle loading was obtained with this methodology.

3.1 Pristine Polyurethane Matrix Characterization

Vials containing ITO nanoparticle powder, and polyurethane solutions with varying ITO content were supplied by Hy-Power Coatings Limited©. A commercial formulation of polyurethane, with unknown composition, is the base of the coating studied in this dissertation. For composition and purity analysis, a dry nanoparticle powder was provided. ITO particles were produced by colloidal precipitation in water using NH_4OH. A ratio of 90:10 In:Sn by weight is expected. Solutions containing 0%, 1%, 3%, 5%, 10%, 15%, and 20% ITO loading were provided to study the effect of nanoparticle loading on coating properties. In addition to polyurethane and ITO, the solutions contain water and dispersing agents. Specifically, ethylene glycol and a carboxylate-PEG are present to keep the nanoparticles from post synthesis agglomeration.

Variable angle spectroscopic ellipsometry data was collected in reflection mode at several angles of incidence. The CompleteEASE [40] software was used to construct a model and to obtain a fit to the measured Ψ and Δ values. The first building block of the model consists of identifying the substrate. All coatings examined with VASE were spin coated on 10mm x 10mm x 0.5mm squares of silicon. The optical behavior of silicon wafers is well characterized, and the dielectric function across the measured range was taken from literature [41]. Similarly, a native oxide layer present on the Si surface has dielectric behaviour obtained from literature [41]. The thickness will actually depend on atmosphere exposure time, storage conditions, and any surface treatments of the Si wafer [42]. The native oxide initially experiences rapid growth but settles into a logarithmic growth after a few hours. A value of 27Å has been approximated for oxides which have been allowed to grow over long periods of time [42]. In modeling, this value was adopted for the oxide thickness without fitting. However, tests were carried out which demonstrated that the resulting model variables were insensitive to the thickness selected.

Prior to the application of the effective medium approximation to the nanoparticle-polymer system, the dielectric dispersion of the polymer matrix was determined. Several samples of the polymer matrix coating, without nanoparticles, were prepared. With the polymer layer present, the model appeared as follows

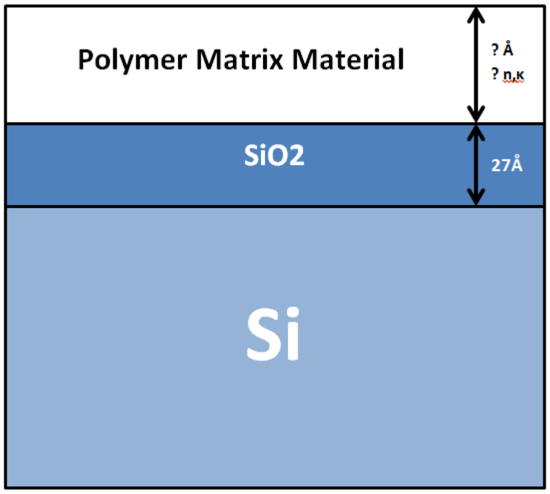

Figure 3.1: VASE model utilized for determining the optical function of the pristine polyurethane matrix.

A multi-sample analysis in the CompleteEASE software allows for several samples to be fitted simultaneously with certain parameters common to all samples and certain parameters unique to each sample. Taking advantage of this feature, several samples can be used to determine the best representation of the dielectric response of the polymer matrix. The index of refraction of the polymer film was defined by a Cauchy function. The Cauchy coefficients were coupled in the model given that all coatings will have the same optical behavior. The only parameter varying between samples is the thickness of the polymer film layer.

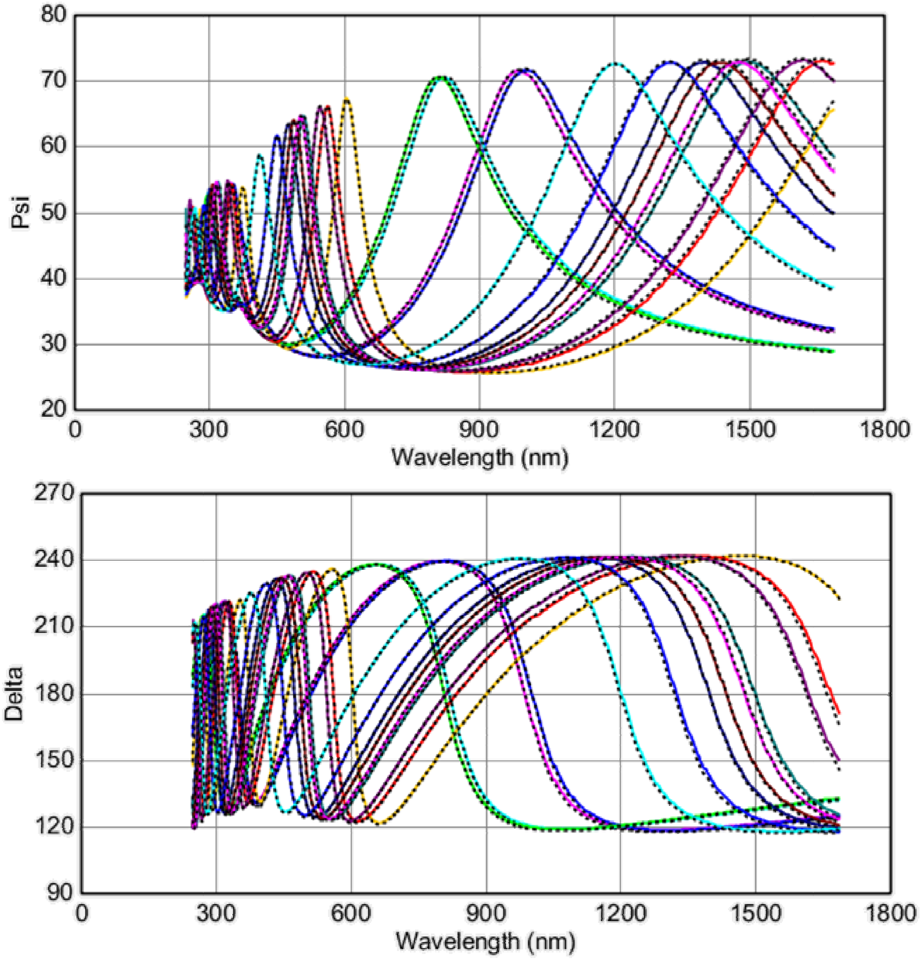

Figure 3.2: The ellipsometry variables Psi and Del versus wavelength for several samples, at an angle of incidence of 56°, for the 3 layer sample (polymer matrix film, native oxide, silicon wafer) system. Experimental values for each sample are represented by a colour curve and the calculated model is represented as the black dotted line for each sample. The model assumes all samples are uniform.

Although the experimental and modeled results display a good fit, there is slight deviation from the experimental Ψ and Δ that is observed in the calculated model result. Thickness non-uniformity is likely the dominant contributor to the misfit. It can be observed by eye that there is variation in colour moving radially from the center of the samples, indicating inconsistency in the film thickness. Including a variable describing the range of the thickness distribution in the model improves the mean square error (MSE) from 19.8 to 13.1. Since CompleteEASE defines thickness non-uniformity as a percentage distribution of the total average thickness, this parameter needs to be fitted individually for each sample.

Comparing the thickness non-uniformity between samples shows a weak increasing trend where thicker samples have the tendency to show more thickness variation.

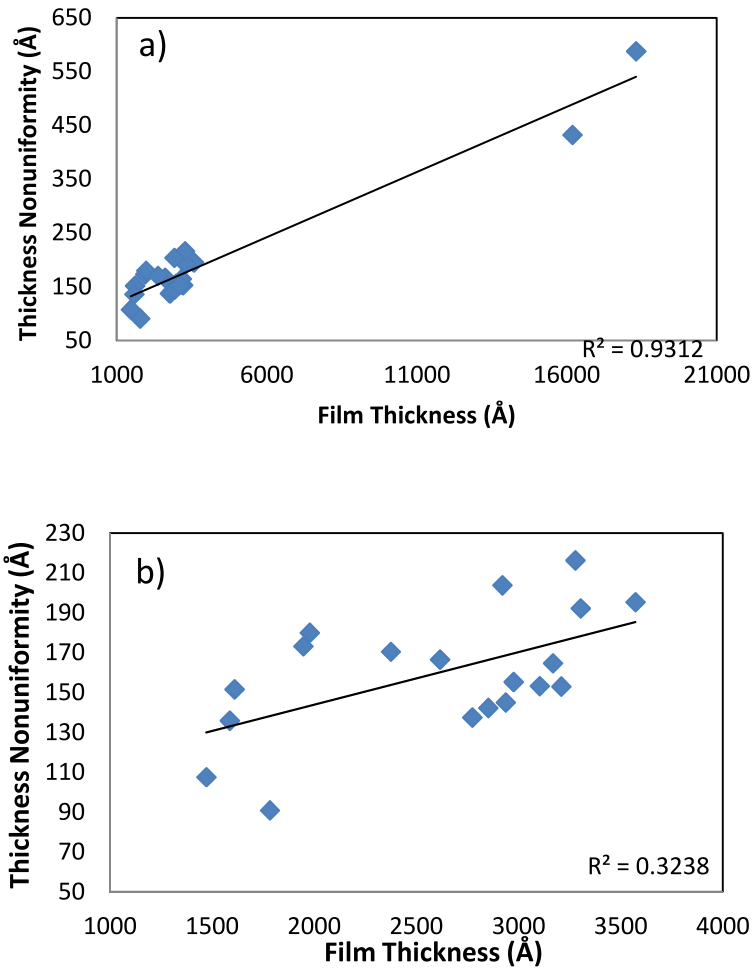

Figure 3.3: VASE modeled thickness non-uniformity for samples with various thicknesses. (a) Showing all sample results, and (b) omitting the thicker samples which were spin cast from the original undiluted solutions.

For samples ranging in thickness between 140-360nm, the average non-uniformity is about 20nm. Samples spun from the received solution, without any dilution, had thicknesses just under 2 microns and a variation of about 50nm. The Cauchy coefficients for the polymer film determined from the 3-layer system with the additional thickness non-uniformity parameter were:

$A = 1.495$ $B = 0.00468\ \text{nm}^2$ $C = 0.000088388\ \text{nm}^4$

and can be applied to Equation 36. The Cauchy function defined with these three coefficients represents the optical response of the polymer matrix material, including all its components such as dispersing agents. The resulting optical constant dispersions are shown in Figure 3.4.

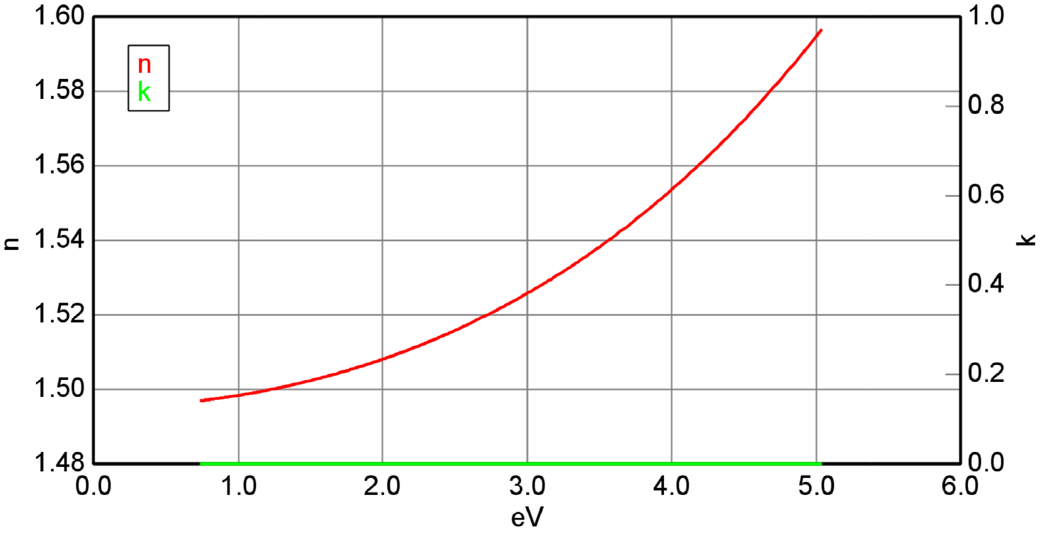

Figure 3.4: Optical function determined from VASE modeling for the polyurethane matrix material. The extinction coefficient is assumed zero in the Cauchy relationship. Generally, polymers have values near zero in the visible energy range.

3.2 Nanoparticle Embedded Film Characterization

The determined optical function for the matrix can now be applied to the model for samples containing nanoparticles. The coating layer will consist of nanoparticles embedded in the polymer matrix, with optical behavior modeled by Bruggeman's EMA. Although many studies exist for the optical characterization of

ITO films [27][39][43], the optical properties of ITO can vary greatly due to differences in structure such as crystallinity, crystallite size, and porosity. In addition, variation in the amount of tin doping and the density of oxygen vacancies will result in optical effects [44]. The fundamental bandgap of ITO occurs in the UV spectral region. Increasing the concentration of tin substituted into indium sites shifts the bandgap to higher energy. Consequently, the deposition technique used for depositing an ITO film will have an effect on the resulting film properties. In addition, since the ITO exists as nano-inclusions in the polymer matrix, quantum size effects will contribute to its optical response. The unknown variables in the model now consist of film thickness, volume % of ITO particles embedded in the film, and the dielectric function of the ITO particles. To reduce the number of fit parameters, it is beneficial to model in a spectral region where the nanoparticles are transparent, i.e. $\kappa=0$. The transparent region for ITO has been identified within the spectral range of 370-650nm [39].

Several samples were measured using atomic force microscopy to accurately determine the surface roughness values. Measuring these values externally allows the surface roughness in the model to be constrained, eliminating it from the fit procedure. Another approach taken to minimize the number of fitted variables was to begin modeling using samples with the same nanoparticle loading, in order to couple the EMA percentage. A percentage of 5% loading was selected for the starting model. Large nanoparticle loadings run higher risk of containing agglomerates, and due to Rayleigh scattering effects on larger particle size, such coatings are not a practical loading for photovoltaic applications. Therefore, creating the starting model with the 20% NP samples would not be representative of an ideal effective medium layer. On the other hand, a low loading will be difficult to detect within modeling error.

Optical behaviour of ITO in the transparent regions can be modeled by the Cauchy relation. Fixing the model range to 370-650nm where ITO is transparent allows the application of the Cauchy model to the ITO nanoparticles. The new model is shown in Figure 3.5 below.

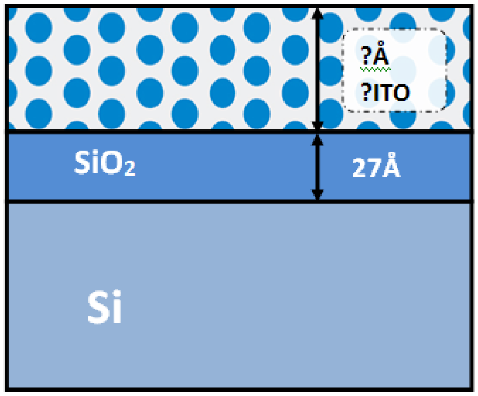

Figure 3.5: VASE model utilized for determining the optical function of the polyurethane matrix with ITO nanoparticle inclusions

To obtain good starting Cauchy parameters, an ITO data file in the CompleteEASE software was parameterized as a Cauchy material in the transparent region. Paramaterizing fits the Cauchy model to the ITO database file, resulting in a function which reflects the data in the database. The Cauchy parameters obtained from the database file would provide close starting values for the Cauchy function for the ITO nanoparticles in the nanocomposite. The resulting coating thicknesses and the EMA volume percent were determined. The volume percent of nanoparticles was found to be 2%. It is expected that the density of the ITO particles will be greater than that of the polymer system, therefore the volume percent calculated by the model should be a fraction of the expected weight fraction of 5%. Before expanding the model to the full spectral range, the thicknesses and EMA % were fixed. By using this approach, the position, amplitude, and broadening of the ITO Lorentz oscillators can be determined without the risk of correlation with other system parameters.

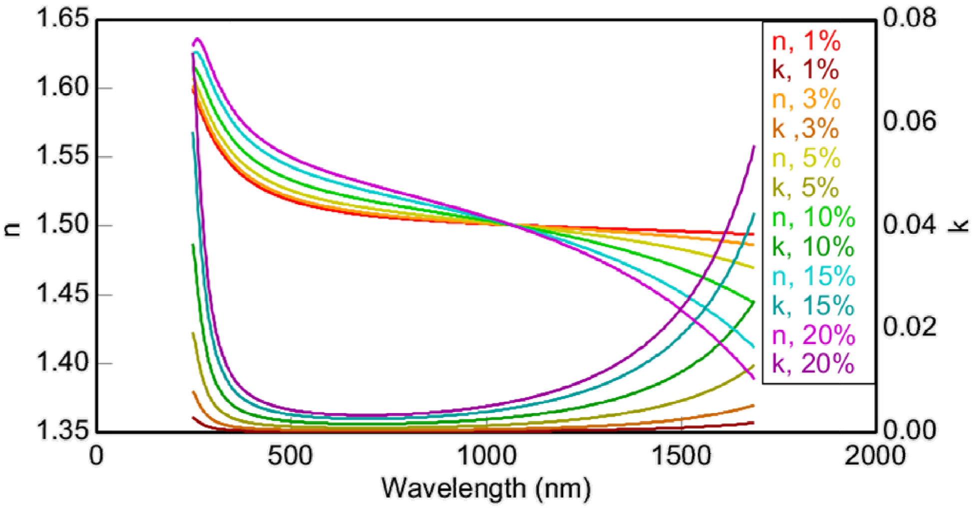

Figure 3.6: Optical functions for nanocomposite films for several nanoparticle loadings. Since the polyurethane matrix, modelled by a Cauchy layer has κ=0, the increase in absorption towards the near UV and IR ranges is due to the ITO inclusions.

The final model can now be used to determine the thicknesses and nanoparticle volume percentage for each of the other loadings. Applying the model, without allowing EMA optical parameters to refine to each loading series separately allows for the coupling of EMA percentage between samples. Average roughness of all samples determined by AFM is approximately 35Å, and can be fixed to all additional samples not analyzed by AFM.

Known Weight %	Modelled EMA Volume %	MSE
1 %	0.3	8.805
3%	0.8	12.407
5%	2	14.874
10%	3.7	21.016
15%	5.9	31.662
20%	7.6	42.664

Table 3.1: Comparison of the final modeled nanoparticle volume fraction to the known weight percentage of the starting coating solution. Modeled values were determined separately for each group of samples, allowing the EMA % to be coupled and the calculation of MSE to indicate the quality of the model fit for each loading

To assess the quality of the resulting optical model, the MSE for each nanoparticle loading is presented in Table 3.1. The error increases with nanoparticle loading. At higher nanoparticle content, the error may stem from reduced transparency of the composite film. Losses from agglomerates may become more pronounced. Also, increasing the amount of nanoparticles randomly distributed in the matrix will increase optical interactions between particles, an effect which is not accounted for in the effective medium approximation.

Another indicator of the quality of the model is the comparison of determined volume percentage of nanoparticles, to the known weight percentage. The mass and volume of a material are directly proportional to one another, observed by the linear trend in Figure 3.7. The resulting volume percent shows good agreement with a linear regression, with $R^2=0.9947$. An intercept of -0.19 for volume percent indicates some error is present. However, this value is not significantly different from zero on a 95% confidence interval (-0.85, 0.47). The error may stem from correlation of variables in the fit, assumptions made in the effective medium model, agglomerate scattering losses, or values chosen for surface roughness and oxide thickness. A systematic approach to reduce correlation effects was taken: however, EMA %, surface roughness, thickness non-uniformity, and ITO absorption all affect the data in the near-UV range. At higher electromagnetic energies, the behaviour becomes more sensitive to surface features. Also, absorption by the nanoparticles and polymer become significant. Therefore, the final fit will be sensitive to the errors in the steps taken to build up the model.

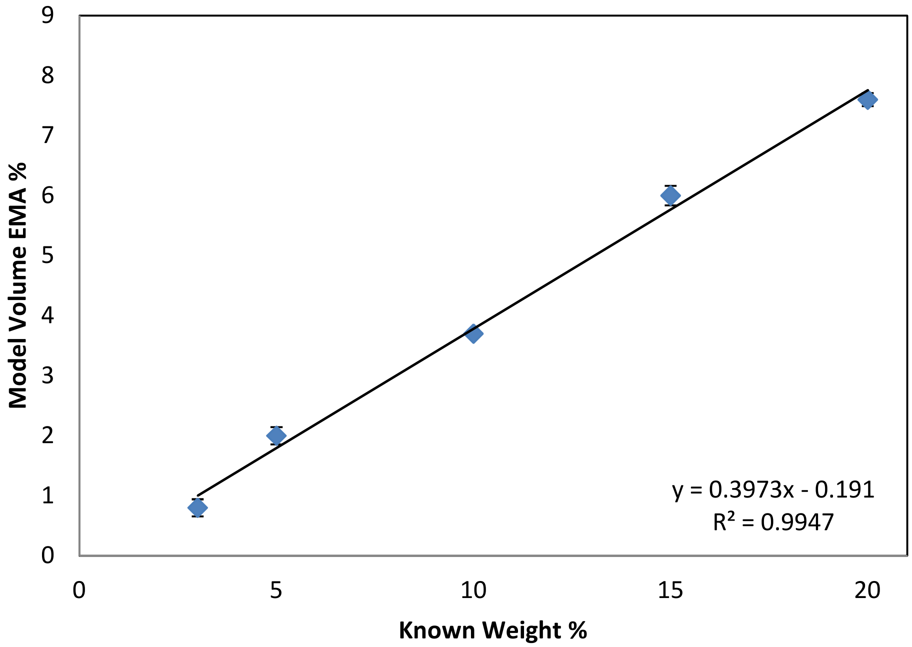

Figure 3.7: The linear relationship of the volume percent from the EMA model with respect to the known starting weight percentage of nanoparticles in the film.

3.3 UV-Visible Spectroscopy

Several films, with varying nanoparticle content, were prepared from non-diluted solutions. The amount of material casted on the glass cover slips was similar for each sample, in order to create films with similar final thicknesses.

The transmittance spectra of the films are found in Figure 3.8. In the visible range, 500-800nm, the composite films showed more than 90% transparency. A decrease in transmittance is observed with higher nanoparticle loading in this energy range. Since the data was collected in transmission mode, the loss of transmitted intensity will originate from both absorption by the sample, as well as reflection off the coating. From the VASE measurement, it was determined that there was a small, but non-zero extinction coefficient in the visible range. Absorption by the coating would account for some of the transmission loss. This would be consistent with the low, but non-zero extinction coefficient found in the

VASE analysis. In the UV-range, the pristine polymer matrix coating showed an onset of absorption near 300nm. With nanoparticles present, absorption starts closer to 400nm. Since ITO is a degenerate semiconductor, the absorption edge is much broader than that of an intrinsic system. For a coating with 5 weight percent of ITO nanoparticles, 20% shielding of UV light at 350 nm is observed.

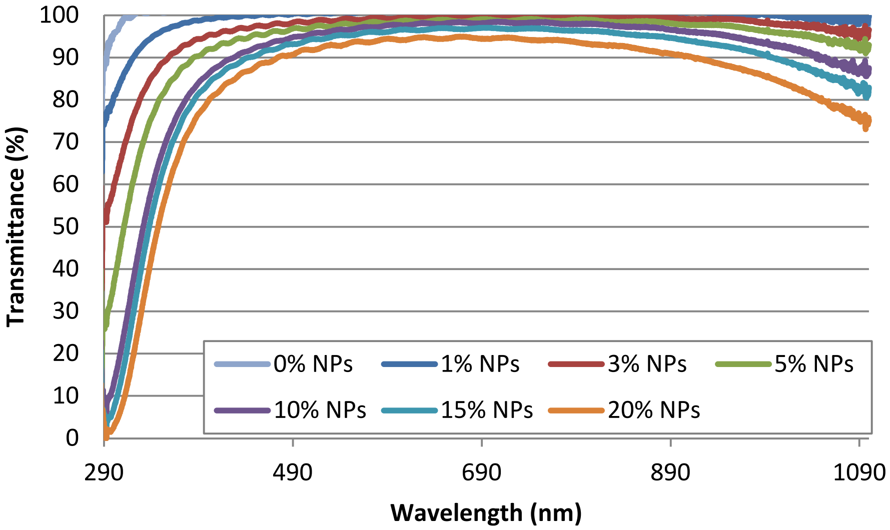

Figure 3.8: UV-Vis transmission spectra for films of similar thicknesses, with different ITO nanoparticle content. High transparency observed in the visible range. Absorption in the UV and near-IR range increased with higher nanoparticle loading.

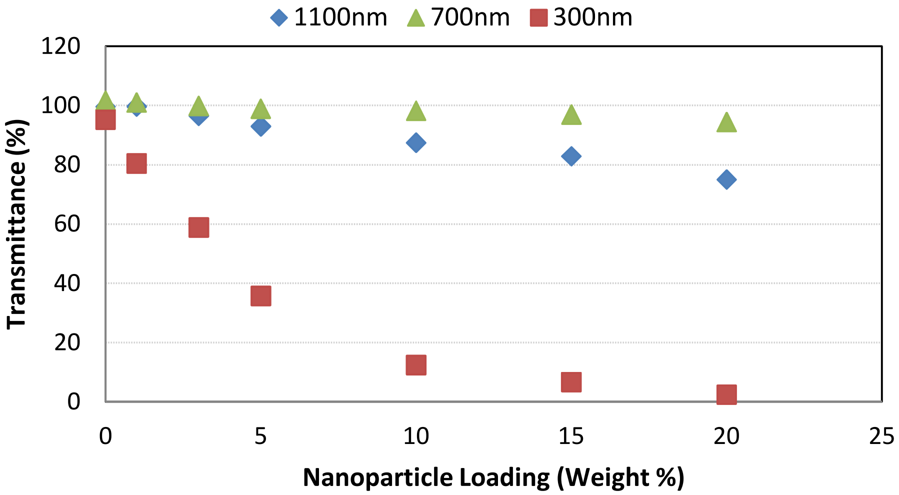

Figure 3.9: The effect of nanoparticle loading on the transmission of light with wavelengths of 1100, 700, and 300nm. Examined films may have varied within a few tens of nanometers. The overall trend shows that UV transmittance is the most affected by nanoparticle loading. In the visible range, near 700nm, the transmittance is not very sensitive to the amount of nanoparticles and remains above 94% for all loadings studied.

The samples which were measured appeared highly transparent with no discolouration or clouding, even with a large nanoparticle loading of 20%. This is an indication that the nanoparticles have good dispersion in the matrix, and scattering losses are minimal. In general, the nanoparticles have the greatest effect on the transmittance approaching the UV spectral range. The sample with 20% loading had only 2.5% transmittance, whereas the 1% nanoparticle loaded sample had 80% transmittance. When considering this nanocomposite system for UV/IR-shielding in solar modules, selection of the optimal loading would involve a balance of the benefit gained from shielding some wavelengths, and the loss from absorption or reflection of useful wavelengths. For example, a Silicon solar cell has an energy bandgap corresponding to 1127nm. When light with a wavelength of 1100nm interacts with a polyurethane coating which contains 5% ITO nanoparticles, the coating transmits 7% less light than if no ITO was present. Light above and near the bandgap is the most efficiently converted into power.

Therefore, the gain in efficiency from keeping the solar module cooler would have to compensate for the 7% of light unable to reach the cell.

Chapter 4: Surface and Nanoparticle Dispersion Characterization

4.1 SEM of Nanocomposite Films

Samples with varying nanoparticle loadings were examined by SEM. Two samples of the 15% nanoparticle loading were prepared with different thicknesses. Sample 1 was approximately 40nm thick and made from an 8:1 dilution from the original mixture. Sample 2 was 300-400nm in thickness, and was prepared from a 3:1 dilution of the same original 15% mixture. The third and fourth sample studied were 5% and 1% loaded respectively, and were both approximately 150nm thick. Samples 3 and 4 were prepared from 5:1 dilutions of their original solutions. Thicknesses were estimated based on their observed colour and the dilution of the starting solution. Each sample was imaged at three different magnifications.

Micrographs were taken on the top surface with a penetration depth on the order of 10s of nanometers. An acceleration voltage of 2kV was applied, and the secondary electrons were collected to produce the topographic images. In the resulting images, the nanoparticles can be identified as the lightest features, and the surrounding polymer matrix material is the grey region. In the topographic images, the particles closer to the surface will appear the brightest, and those embedded deeper in the film will appear greyer. The back-scatter electron images are shown in Figure 4.2. These images were collected with an acceleration voltage of 5keV and show compositional variations in the film. The particles were uniform in their light grey colour, supporting that all the particles have the same composition.

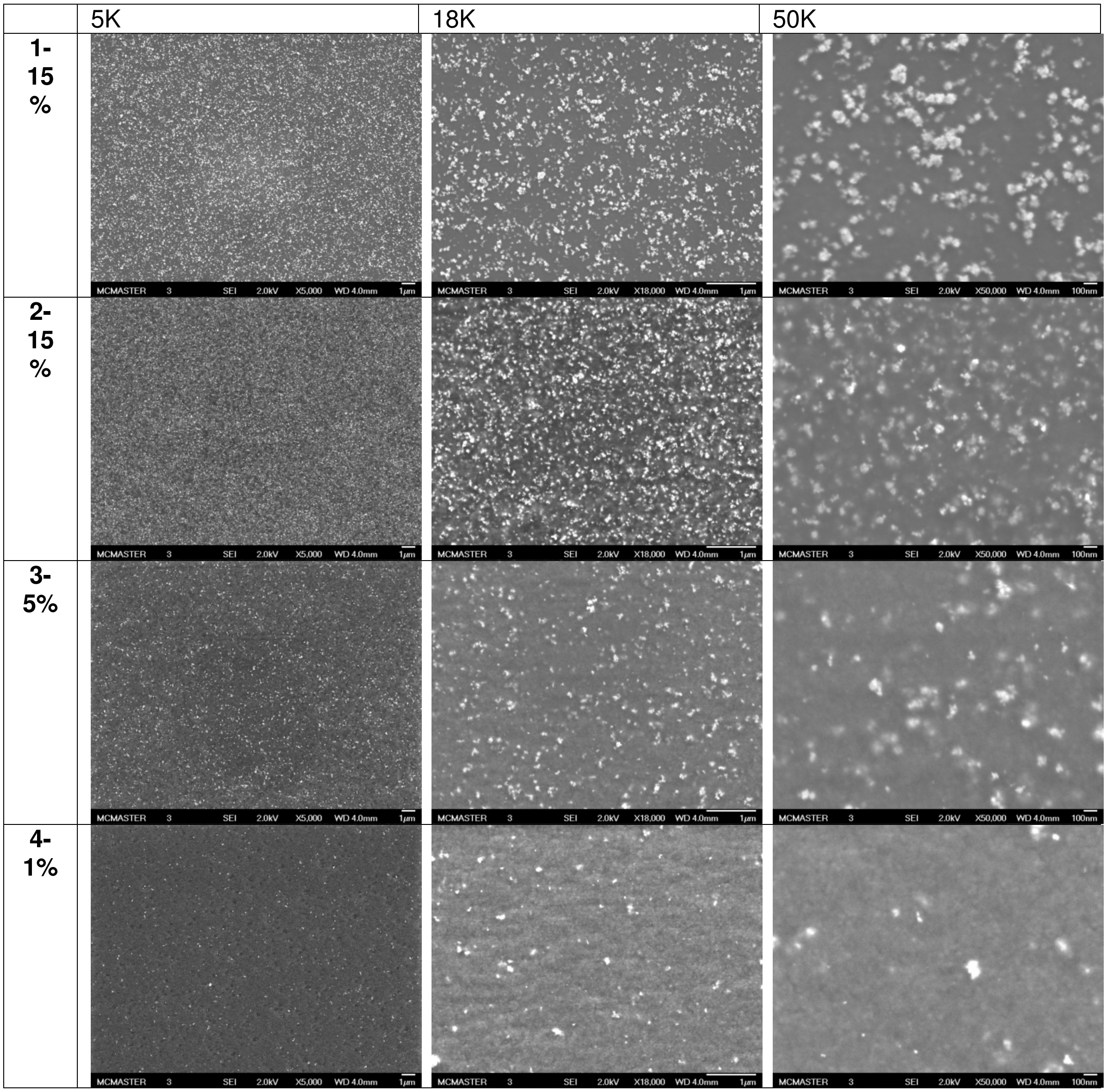

Figure 4.1: SEM images of polyurethane nanocomposite films with 15%, 5%, and 1% weight percent of ITO nanoparticles. Films were examined at three different magnifications: 5K, 18K, and 50K times. Films spun from starting solutions of higher nanoparticle concentrations showed larger nanoparticle density. Two films with 15% nanoparticle loading, with different film thickness were compared. The thicker film, Sample 2, appears to have a higher nanoparticle density. The topographic images do not provide information on the distribution of nanoparticle with respect to film depth.

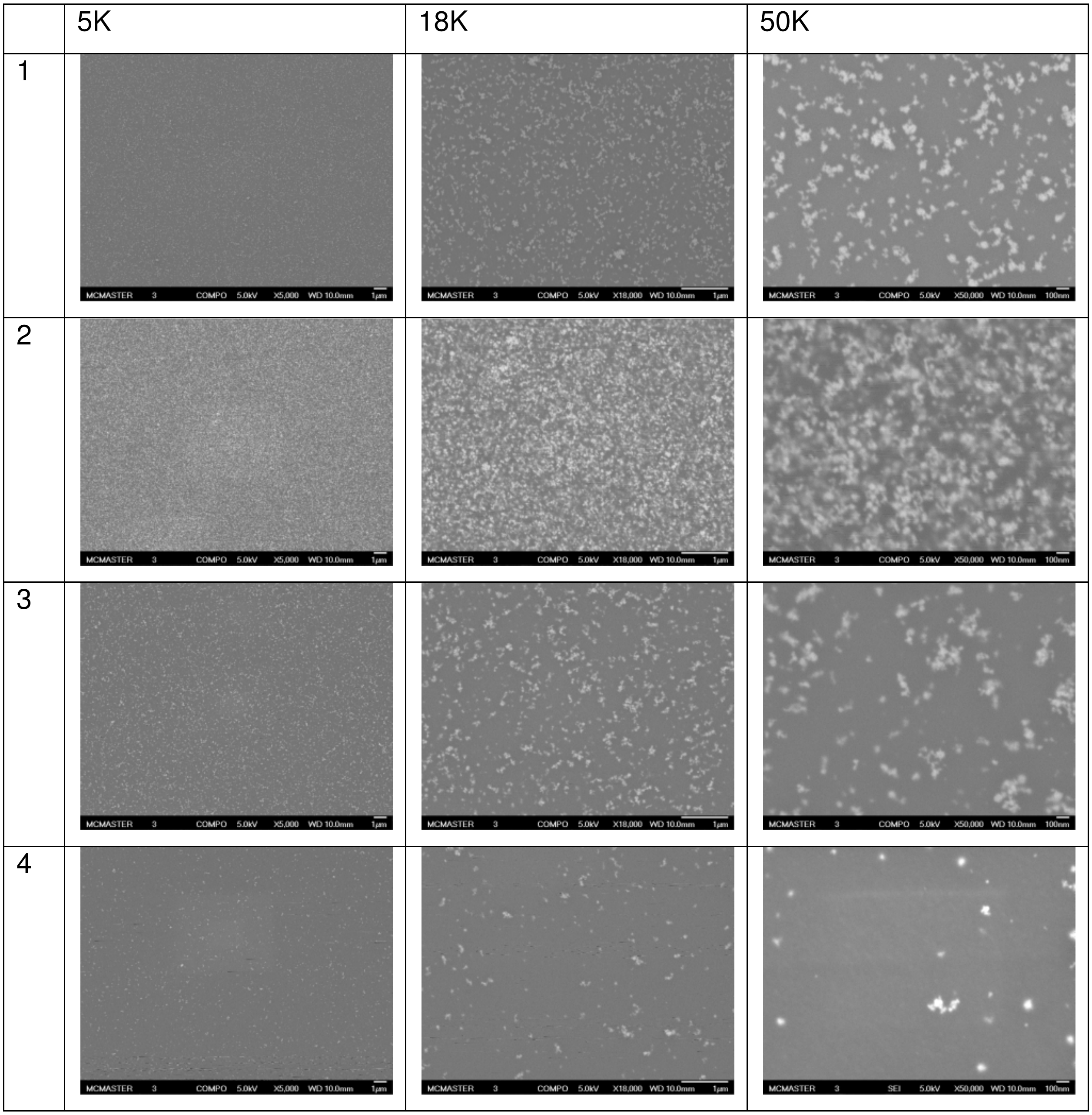

Figure 4.2: Back-scatter electron images showing variation of composition in the nanocomposite coating.

It can be observed in the images that particle density decreases with a decrease in nanoparticle loading, as expected. An important feature to note is the presence of agglomerates. It appears as though the majority of the nanoparticles exist in clusters as opposed to ideal single particles. Without the depth dimension available, accurate agglomerate size estimates are difficult to make. Rough size measurements result in a range of 20-110nm in diameter. Single nanoparticles are easier to identify in Sample 4 because of its lower nanoparticle loading. Also, to more easily identify particle boundaries, the back-scatter electron images were used for measurements. It is apparent that the amount of agglomeration decreased with lower nanoparticle loadings, although this is to be taken with caution for topographic images since the clusters observed may actually consist of independent particles at varying depths. Particles which appear to be single ITO particles were approximately 15-25nm in size.

Another feature which can be observed qualitatively in the images is the surface roughness. Sample 1 and Sample 2 both had 15% nanoparticle loading but were prepared with different dilutions. Sample 2 had a lower dilution, and as a result, was much thicker than Sample 1. Taking a look at the topographic images, it appears as though Sample 2 exhibits some three dimensional texturing. As mentioned earlier in this chapter, features closer to the surface will appear lighter in colour. Variations in the shade of grey in the matrix suggest that the surface is uneven. The texturing looks more prominent than what is observed in Sample 1, the thinner sample. Another observation made was that the matrix of Sample 4, with only 1% nanoparticle concentration, experienced thermal damage during the analysis. While under the active electron probe, the polymer matrix was changing shape. This occurrence can be explained by lower thermal conduction due to lower nanoparticle concentration. ITO is known to be very stable, and has the ability to tolerate voltages greater than 1000V when in solution or embedded in polymer films [45]. Therefore, it is expected that the nanoparticles were not damaged by the electron beam.

4.2 TEM of Nanoparticle Powder

A vial containing a dry indium tin oxide (ITO) nanoparticle powder was supplied by Hy-Power Coatings Limited©. Although a great amount of detail was not provided, it is known that the ITO particles were produced by colloidal precipitation in water using NH_4OH. A ratio of 90:10 In:Sn by weight is expected based on the starting stoichiometry.

To investigate the physical features of the ITO nanoparticles, such as size and morphology, the powder form was characterized by TEM. Preparation of the sample started with the powder added to ultra-pure water and sonicated for several minutes to disperse the particles. A drop of the mixture was placed on a copper TEM grid. To support the fine particles, the TEM sample grid had a carbon film.

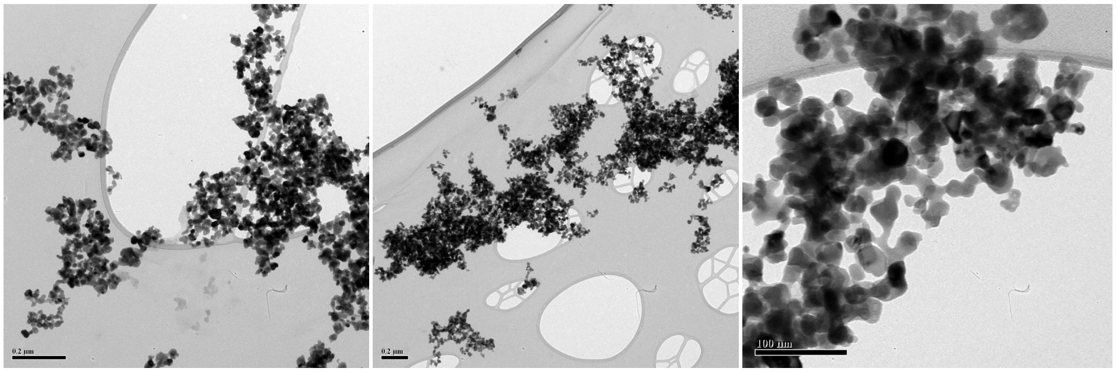

Figure 4.3: TEM images of nanoparticles deposited on a copper grid having a carbon support film. Particle isolation was not accomplished, and particles are found in large clusters along the grid surface.

Images were collected at low magnification to observe the general spread of the particles deposited on the carbon film. The film is identified as the medium grey tone comprising the majority of the background. The pores in the film are the lightest grey, and the particles are the darkest features. Clusters are present throughout the examined areas, with individual isolated particles difficult to locate.

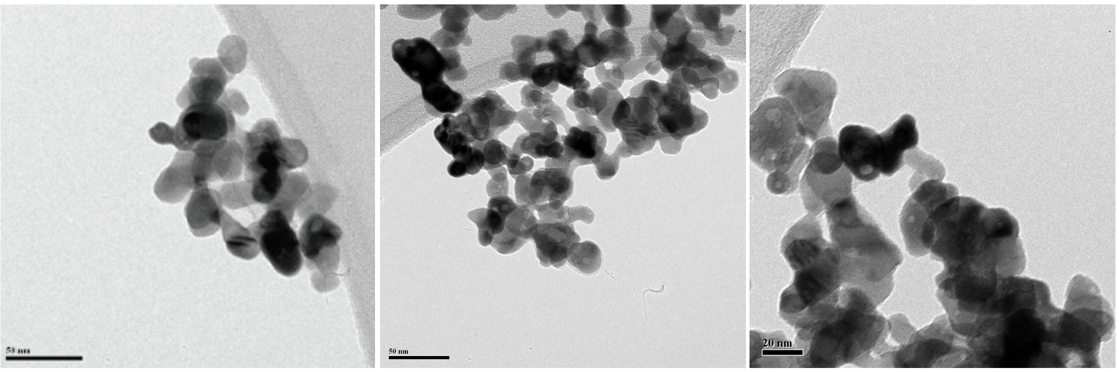

Figure 4.4: High magnification TEM images of nanoparticle powder. Particles appear in clusters, with only a few definable particles observed.

Higher magnification imaging was applied in an attempt to focus in on individual particles. The particles are not perfectly spherical in shape, instead appear oblong and some have a characteristic bean shape. Several features should be noted. Firstly, there are areas of amorphous material that appear to connect several particles. Secondly, there are particles which exhibit a series of parallel dark lines traversing the particle. In TEM, these are characteristic of diffraction lines, indicating the crystallinity of the material. A third observable feature is the presence of numerous small roughly circular structures. They appear to be located in or on the surface of the particles, but the exact association cannot be distinguished in the images. A final feature worth mentioning is a rough outline of material surrounding several particles.

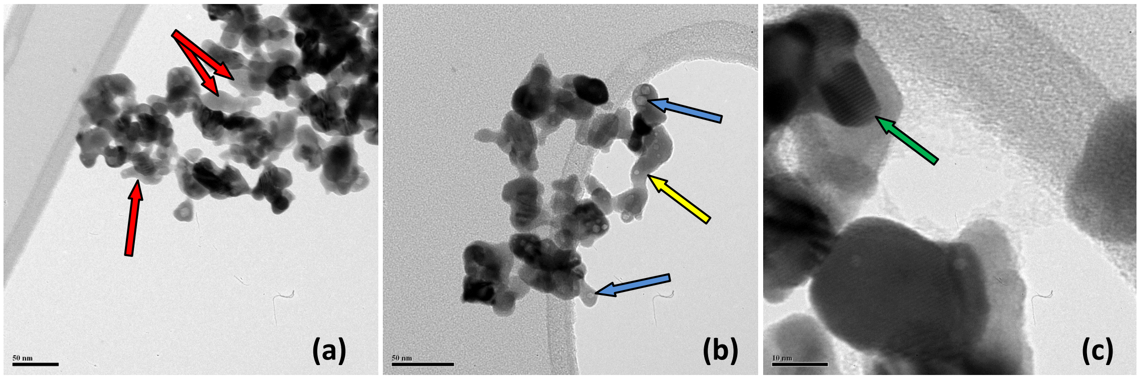

Figure 4.5: Higher magnification images from TEM showing various features. In (a), amorphous regions are indicated with red arrows. With blue arrows, small

circular structures are indicated in (b). A green arrow points to lattice fringes in (c). Connecting material is shown with a yellow arrow in (b).

The particles were oblong in shape. To determine the average particle size, 15 particles were measured along the short and long particle axes. The average dimensions were 18x25nm. This is in good agreement with the estimated size from Section 4.1. The average diameter of the small circular structures indicated in Figure 4.5(b) was 5nm, as determined from averaging the dimensions for 10 structures.

4.3 Energy Dispersive X-ray Spectroscopy

For the elemental analysis of the nanoparticles, energy dispersive x-ray spectroscopy (EDX) was used. During an EDX measurement, the specimen is exposed to a high energy beam of protons, electrons, or x-rays, which induce excitation of core electrons. Atoms in the material will have electrons at discrete energy levels. The excitation source induces a transfer of an electron to a higher energy state, leaving behind an empty state or a hole. An electron from a higher energy state will relax down to fill the hole, emitting an x-ray with a characteristic energy. The resulting spectrum after the measurement contains information on both the energy and number of x-rays the specimen emits. The energies of the x-rays identify the type of elements present, and the relative intensities of x-rays at each of the observed energies are used to determine the atomic weight percent of each element.

For bulk analysis, the ITO nanoparticle powder was pressed into a thick film onto a piece of carbon tape. The measurement was performed with an Oxford Synergy EDX system integrated into the Jeol JSM-7000F SEM instrument. A second set of measurements was obtained with an Oxford EDX spectrometer built into a Philips CM12 TEM instrument. Initially, the objective of the second measurement was to determine the variation in composition between individual particles. Since single particles resulted in poor counting statistics, several particle clusters were studied instead.

The result for the qualitative EDX analysis of the bulk pressed specimen is found in Table 4.1. According to the results, the ITO had 6.5% tin doping. The data represents an average elemental composition of many particles. Other elements also found in the sample are nitrogen, potassium, and traces of silicon. These may be contaminants. If the nanoparticles are functionalized to improve miscibility with the polyurethane, these may be some of the elements found in the functional groups.

Element	Weight %	Atomic %
N K	2.73	8.07
O K	25.05	64.75
Si K	0.31	0.45
K K	1.26	1.34
In L	65.90	23.73
Sn L	4.74	1.65
% In/Sn		**93.5/6.5**

Table 4.1: Average composition of bulk pressed powder examined using EDX.

To observe any variation in the composition between particles, EDX analysis of five clusters was done. The clusters consisted of 3-10 nanoparticles. Measurement of clusters was chosen over single particles in order to improve the signal response. The resulting data is displayed in Table 4.2. The average tin content for the five examined clusters was 8.4%. The clusters showed differing amounts of tin. Although the variation is on the order of a few percent, the implications should be noted. It has been found that the SPR frequency is dependent on the tin content in ITO [45]. Increasing the amount of tin from 3 to

10% was reported to blue shift the SPR peak by approximately 600nm. This may be critical in some optoelectronic applications. However, for UV/IR shielding coatings, the different SPR responses would increase the IR spectral coverage, and thus improving the IR shielding. A possible explanation for the varying compositions between clusters is that there are indium or tin atoms which may not necessarily be part of the ITO system. Features observed by TEM, noted with arrows in Figure 4.5, may contain some excess tin or indium.

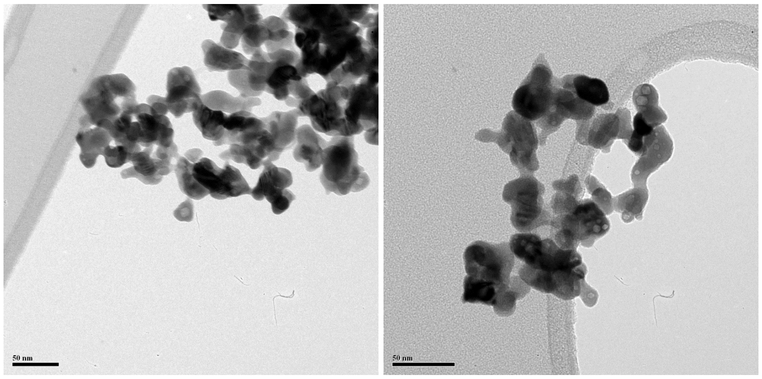

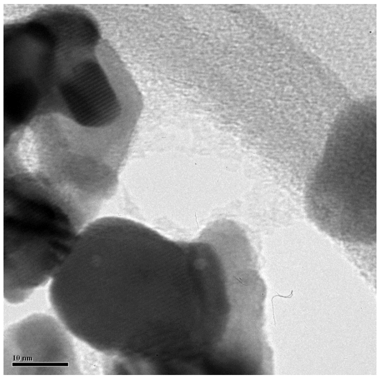

Cluster	Oxygen	Indium	Tin	% In/Sn
1	75.80	22.07	2.13	91/8.8
2	75.96	22.76	1.27	94.7/5.3
3	75.03	23.01	1.96	92.2/7.8
4	75.57	22.77	1.66	93.2/6.8
5	71.45	25.03	3.52	87.7/12.3
Average	**74.76**	**23.13**	**2.11**	**91.6/8.4**

Table 4.2: EDX compositional analysis of ITO nanoparticle clusters. Values pertain to elemental composition of ITO.

The average fraction of indium to tin determined by the bulk measurement was lower than the average for the analysis of several clusters. However, it lies within the standard deviation of the original result. The elemental composition is determined by a peak deconvolution method. Tin and indium have peaks which partially overlap, and thus, there exists some uncertainty in the resulting values. The calculation is automated on the SEM system used.

4.4 TEM of Nanoparticle Embedded Films

Very thin films, on the order of tens of nanometers, were prepared by first diluting the original mixtures to 8:1 with ultra pure water. After dilution, the samples were dispersed in a high speed shaker for about a minute. Films were spun on freshly cleaved mica substrates. The resulting three films, with 15%, 5% and 1% loading were approximately 40-60nm thick. The films were floated off into a water bath and picked up by a TEM grid. The orientation of the film was noted, such that the free surface of the originally spun film corresponded to the top of the TEM grid surface. Images were taken at three different magnifications for each sample.

1%	5%	15%
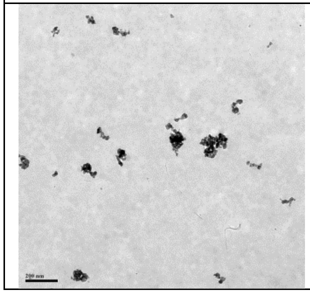	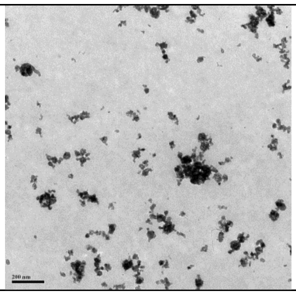	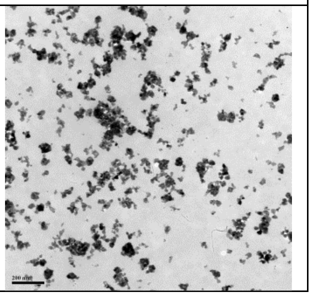

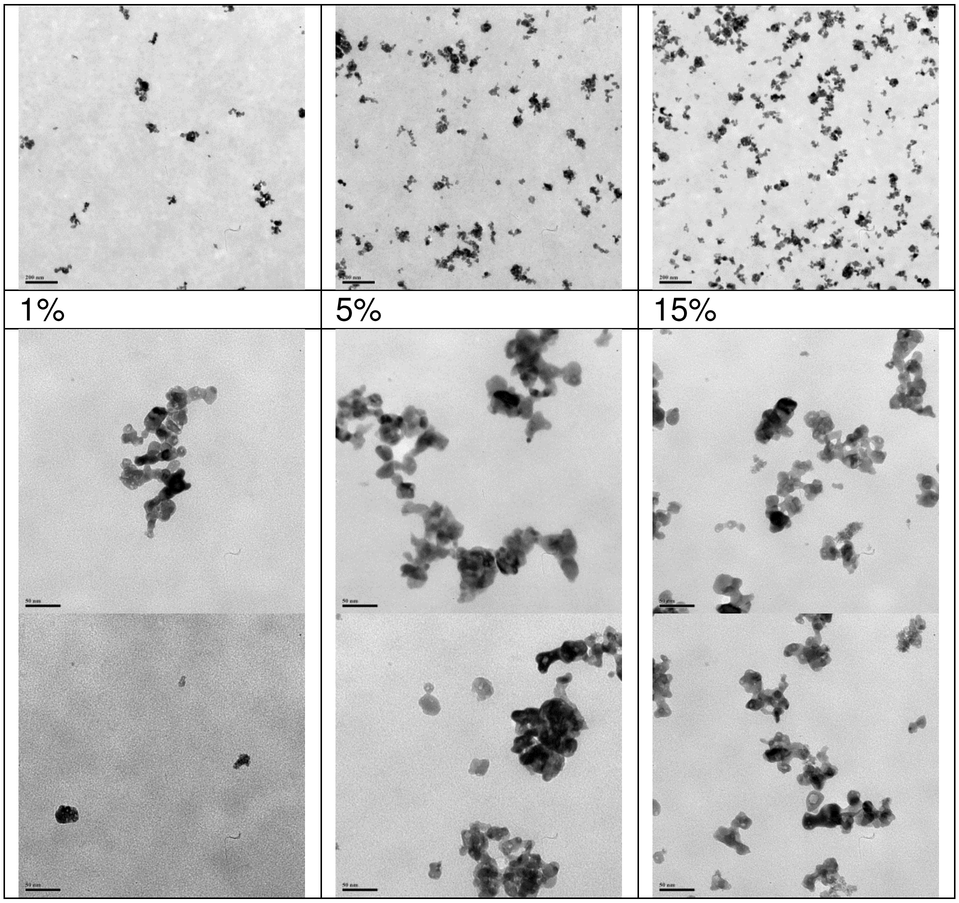

Figure 4.6: TEM images of floated thin films made from solutions of 1%, 5%, and 15% nanoparticle loading. Top images are at low magnification, and the lower six images are at higher magnification. Images are obtained looking through the film's surface normal at different magnifications.

Similar to the previous TEM images done on the nanoparticle powder discussed in Section 4.2, the particles appear as the dark features, and the polymer matrix is the surrounding light grey area. In the low magnification images, there is a preferential existence of nanoparticles in clusters, similar to what was observed in the powder images. The clusters vary in size, and are found in all of the images. Clusters average between 30-240nm in size. The agglomerates approach dimensions which are comparable to the thickness of the film.

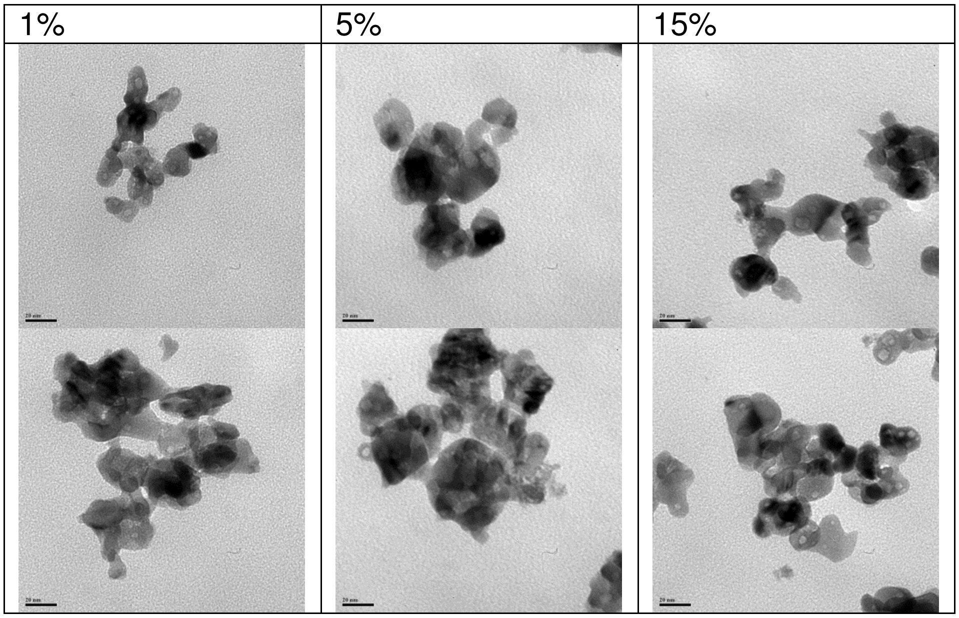

Figure 4.7: High magnification TEM images o nanoparticle clusters.

An increase in magnification provides more detail on the shape of the clusters. A few isolated nanoparticles can be identified in the images. The average particles size, as determined from the measurement of 10 particles, was 16±4nm. Some texturing in the polymer matrix is also observable at this higher magnification.

4.5 TEM of Microtomed Nanocomposite Films

The same preparation of the nanocomposite films was performed for several 5% ITO films as mentioned in Section 4.4. Once the films were floated in the water bath, two polystyrene beads, which had been softened using a toluene soak, were pressed together with the film situated in between. The polystyrene layers form a rigid support on the thin films, which are then microtomed into manageable segments for TEM examination.

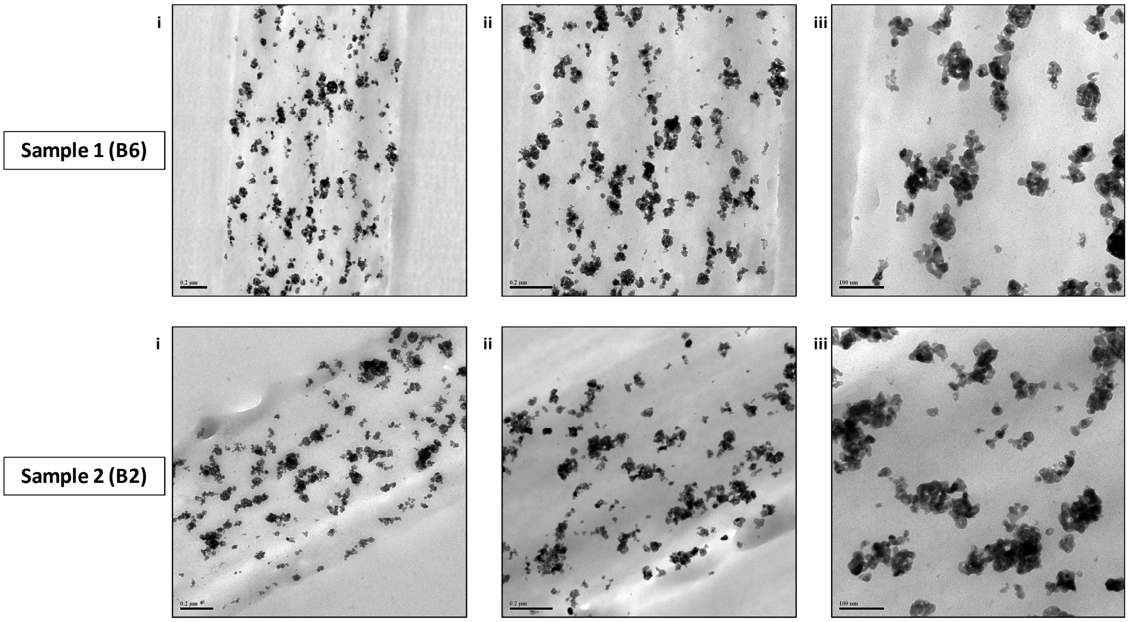

Figure 4.8: Cross-sectional TEM imaging of nanocomposite films for two segments.

Images for two segments, Sample 1 and Sample2, are displayed in Figure 4.8. The distribution of nanoparticles in the matrix is best identified in the low magnification images. Similar to the observations made in Section 4.4, the nanoparticles are more commonly found in agglomerates or clusters and not as single entities. The largest cluster was measured to have the longest dimension of 230nm. A few clusters are found close to the interfaces, however, the general distribution appears random. There is no evidence of nanoparticle segregation in the spin coated films at room temperature. Studies carried out to investigate if heat induces segregation are found in Chapter 5.

4.6 Atomic Force Microscopy

The topography of an optical coating will have an influence on the behavior of light incident on the surface. Surface measurements were obtained by atomic force microscopy (AFM). Multiple areas on a series of samples were examined to determine the root mean square (RMS) and average roughness. Surface roughness is one way to quantify vertical deviations in the actual surface from ideal. Values expressed in terms of the root mean square will be more sensitive to extreme surface anomalies than the average values.

Two to six spots on a total of 11 samples were measured. The samples examined were a subset of those previously examined by spectroscopic ellipsometry, described in Chapter 3. The average measured AFM values were also applied to the VASE modeling in that chapter. Surface measurements were performed in tapping mode using a Caliber atomic force microscope made by Veeco. The scanning rate was 0.35Hz for the majority of the measurements. Some measurements were done at faster rates, up to 0.75Hz. The scan size was also varied but 5µm was used for many of the runs.

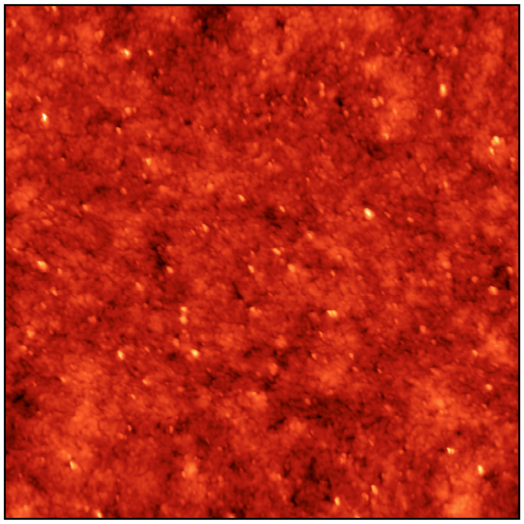

Figure 4.9: Topographic image of a 20% nanoparticle loaded nanocomposite coating spin cast from a 2:1 diluted solution. The image spans 5 microns across. Surface texturing and nanoparticles are apparent.

The average roughness for the clear polyurethane coat spin cast from a 2:1 diluted solution with no ITO nanoparticle present was 2.4nm. The RMS roughness was 3.1nm, slightly larger than the average. For a very coarse surface, with more extreme peaks and valleys, the RMS value will be much higher than the calculated average. A similar difference between the two calculated terms is observed for all samples measured, as can be seen in Table 4.3. A general trend shows that the roughness increases with nanoparticle loading. The trend is observed in Figure 4.10. Although it is expected that the nanoparticles will influence the spin casting dynamics, and therefore potentially the resulting surface, it is unexpected that the 20% loading samples would show lower surface roughness. Loadings from 0-10% show increasing roughness with increasing nanoparticle loading. Better counting statistics involving more samples would be required to determine if the 20% sample is an outlier. In addition, sample variables such as solution concentration would need to be considered. An image of one of the 20% AFM measurements is found in Figure 4.9. Surface texturing and nanoparticles are evident.

Sample	Dilution	RMS Roughness (nm)	Average Roughness (nm)
clear	2:1	3.11	2.44
1%	1:1	4.07	3.14
	5:1	4.29	3.30
3%	2:1	4.34	3.38
5%	1:1	5.02	3.80
	2:1	5.00	3.83
	3:1	5.73	4.21
	5:1	5.82	4.0921
10%	2:1	6.36	4.7633
20%	2:1	4.71	3.6177
	5:1	5.53	4.0641

Table 4.3: Average surface roughness measurements by atomic force microscopy for several samples with varying nanoparticle loadings and thicknesses. RMS and average values obtained by averaging the values determined from several locations on the same sample.

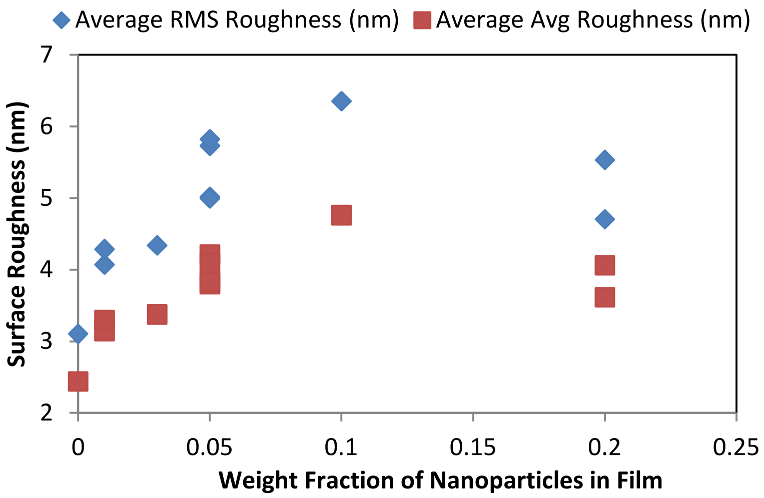

Figure 4.10: The effect of nanoparticle loading on the resulting surface roughness.

Chapter 5: Thermal Dependence

In field applications, the coating would be exposed to a range of temperatures, thus it is important that the matrix remains stable within this range. To study the thermal behaviour of the polyurethane matrix, differential scanning calorimetry (DSC), thermogravimetric analysis (TGA), and ellipsometry were used. Depending on the composition, polyurethane materials have shown different responses when heated. The polymer matrix examined here is made from an aqueous dispersion of polyurethane (of unknown composition) and dispersive agents. It is expected that initially, when the system has not reached an equilibrium state, significant rearrangement and irreversible transitions would occur. Taking sequential measurements will demonstrate this, as well as reveal any reversible transitions such as melting temperatures and glass transitions.

5.1 Introduction

Alternating block copolymers, such as polyurethanes, exhibit complicated thermal behavior. As mentioned in Section 2.3, miscibility between the two different segments as well as structural ordering between similar segments will influence the properties of the system. Due to the different chemical affinities of the segments, the formation of segment domains may occur. Hydrogen bonding plays a major role in domain separation, creating crosslinking networks. With regards to the thermal response, the hard and soft segment may each have glass transitions, melting endotherms, or crystallization exotherms which take place at different temperatures. However, one may be suppressed or shifted depending on the type and extent of another. These complexities lead to the difficulties found in interpreting polyurethane systems.

Extensive research in the thermal stability of polyurethane has established general trends based on system variables such as segment length, composition, and molecular weight.   Changing the fraction of hard segment to soft segment, indicated by the NCO/OH content ratio, was found to shift the melt endotherm (T_m) of the soft segment [46]. As the hard segment content increases, the amount of crosslinking increases, eventually to the extent that the soft segment can no longer flow freely. This leads to the absence of the soft segment melt endotherm. Changing the isocyanate group, known as the hard segment of polyurethanes, has shown to change the glass transition temperature of the soft segment. An aromatic hard segment makes crystallization of the soft segment difficult, resulting in the absence of a T_m for the soft segment. Some hindering of soft segment crystallization was also found with aliphatic isocyanate, concluded from the decrease in ΔH_m compared to the corresponding polyurethane form with no hard segment present [47]. In systems which are capable of hydrogen bonding, an increase in the amount of hard segment decreased the degree of domain separation [48]. The more intricate cross-linked network that forms when there is more hard segment prevents the arrangement of the segments into separate domains.

5.2 Differential Scanning Calorimetry

Four samples were prepared for the DSC study. The first two DSC aluminum pans contained drops of the 5% NP loaded, undiluted mixture. The other two pans had the undiluted, matrix mixture only. To evaporate the water prior to measurement, the pans were heated on a hot plate set to 120℃. The samples were frequently stirred to facilitate the process. Once the samples appeared dry, they were transferred to a vacuum oven where they were held at 110℃ for 6 hours. The oven was then turned off, and the samples remained in the oven as it slowly cooled for 17 hours. Differential scanning calorimetry (DSC) measurements were done using a TA Instruments model DSC2910 with a standard cell attachment , using standard aluminum sample pans. Samples were heated from -60℃ to around 200℃ at 5℃/minute in a nitrogen environment.

DSC data for several consecutive runs of each sample was obtained. The resulting heating curves are shown in Figure 5.1. Comparing samples, some notable similarities can be observed. During the first run for all four samples, a broad endotherm with transition onsets occurring between 27-38°C, and transition temperatures between 45-85°C are observed. These transitions span somewhere from 65-100°C, with some limits difficult to define due to the complicated behaviour of the polyurethane material. With following runs, a decrease in the change in enthalpy is seen until the endotherm is essentially no longer apparent. Possible reasons for this behaviour include hindering of soft segment melting, annealing induced ordering, varying thermal history, and absorbing of water.

The disappearance of the endotherm is characteristic of the soft segment melting being suppressed as the overall structure becomes more rigid. The mobility of the soft segment located between hard segments is reduced because of the increase in hydrogen bonding between NH and C=O groups surrounding it. This occurs when miscibility between segments is high, and segmental domains are no longer present. A second possible explanation for the broad endotherm is an irreversible structural rearrangement as the system goes through an annealing induced ordering. Woo et al. [49] explained the phenomenon by the effect of hydrogen bond dissociation between segments, allowing for the reconfiguration of the polymer matrix. In previous work [50], it was shown by FT-IR spectroscopic monitoring during isothermal annealing that the N-H stretching absorption band varied with time. Since all four samples underwent annealing prior to the DSC measurements, irreversible annealing processes may have already occurred. The third possibility involves the influence of thermal history on the behaviour of polyurethanes. Yoon *et al.* [50] have observed different rheological responses in a polyurethane thermoplastic, depending on thermal history. Considering the history of the material directly before measurement, it may be that hysteresis causes consecutive runs to vary from the first run. After annealing in the vacuum oven, the samples were left to cool slowly overnight. On the other hand, after the completion of run 1, the sample was cooled rapidly in order to prepare for the second run. Rapid cooling, or quenching, prevents or hinders the material from undergoing the reverse transitions from those found in the heating process. The final possible explanation discussed here is the effect of humidity on the samples. If the material is hygroscopic, it will absorb water out of the air when exposed to a humid environment. The sample was in air when placed into the DSC instrument. During the measurement, the sample was in a nitrogen environment, with no water. To help isolate the cause of the irreversible transition occurring between 65-100℃, another series of DSC measurements were conducted. A discussion of the experiment and results are found at the end of this section.

Sample	Onset Temperature	Transition Temperature	Width of Transition
1	37℃	46℃	66℃
2	31℃	45℃	67℃
3	29℃	85℃	101℃
4	30℃	78℃	83℃

Table 5.1: Characteristics of broad transition found in the first run of all 4 samples.

In the temperature range -20 to 30℃, inconsistent endotherms and exotherms appear between runs. The key features are noted in Table 5.2. Sample 1 experienced several exothermic transitions. Exothermic transitions are typically crystallization events. The transitions are indicated by two consecutive peaks in runs 1 and 2, and the peaks occur at the same temperature. The change in enthalpy lowers in run 2. After the crystallization exotherms in run 2, a sharp endotherm at 29℃ appears. This can be correlated with the melting of the crystalline soft segment. Interestingly, the following run did not show an exotherm. It is as though melting drove the ordered soft segment into a new disordered configuration. This can be indicative of improved mixing of hard and soft segments. During the fourth run, a convoluted pair of crystallization exotherms appears around 20℃ lower than in the first two runs. The second run of Sample 4 exhibited a single exotherm at 2℃.

Due to the malleable nature of the soft segment, its characteristic thermal transitions often occur at lower temperatures. Hartmann et al [34] observed the soft segment glass transition occurred between -71 to -3℃. In the same work, polyurethanes that showed a melt endotherm for the soft segment, it occurred between 3 to 22℃. Thus, it is suspected that the lower step deflection corresponds to glass transitions occurring in the material, and the higher temperature endothermic peaks between 22-29℃ correspond to melting. Endotherms near zero degrees Celsius are attributed to water freezing in the system. In general, the majority of the runs for all samples show that the melt endotherm peaks are either much less apparent, or are not present at all. Weak melt endotherms indicate that the polyurethane segments exhibit elastomeric behaviour with homogeneous mixing of hard and soft segments [51]. It has also been found that when hard segments and soft segments show some miscibility, shifts in temperature of the thermal transitions may occur upon several temperature runs [47].

Sample #	Run #	Exothermic Peaks	Endothermic Peaks
1	1	1℃, 7℃	-
	2	1℃, 7℃	29℃
	3	-	18℃, 22℃
	4	-17℃, -15℃	-
2	1	-	-9℃, 23℃
	2	-	11℃
	3	-	-12℃, 26℃
3	1	-	-7℃, 6℃, 22℃
	2	-	-17℃
	3	-	-13℃, 12℃
4	1	-	0
	2	2℃	-3℃
	3	-	3℃

Table 5.2: Key low temperature transitions. The appearance of sharp exotherms is inconsistent. The temperature at which the exotherms and endotherms occur is variable, with a few common features between runs.

Since the polymer matrix contains ethylene glycol as a nanoparticle dispersant, some features may be associated with freezing of the ethylene glycol. Ethylene glycol is known for its dependency of freezing point on the concentration in water, as used in antifreeze. Freezing can vary from -60 to 32℃ depending on the dilution. Similarly, the interactions of ethylene glycol with the polymer matrix may be complicated and freezing endotherms may occur more erratically. In a similar way, the interactions of the ethylene glycol may also influence the behaviour of the polyurethane.

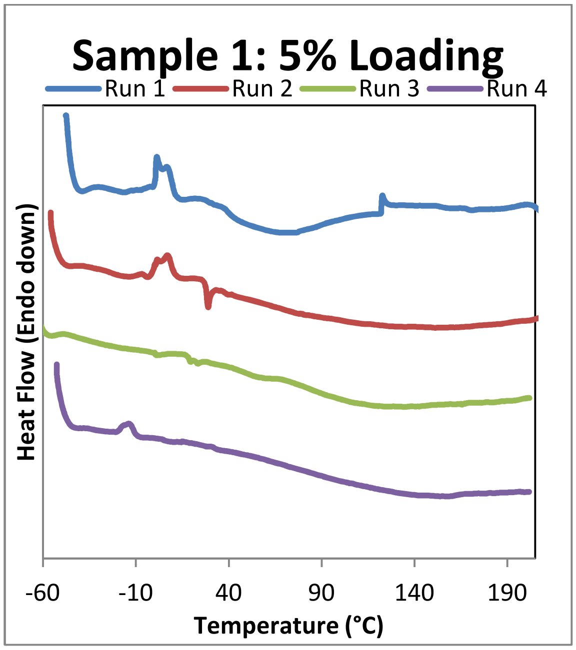

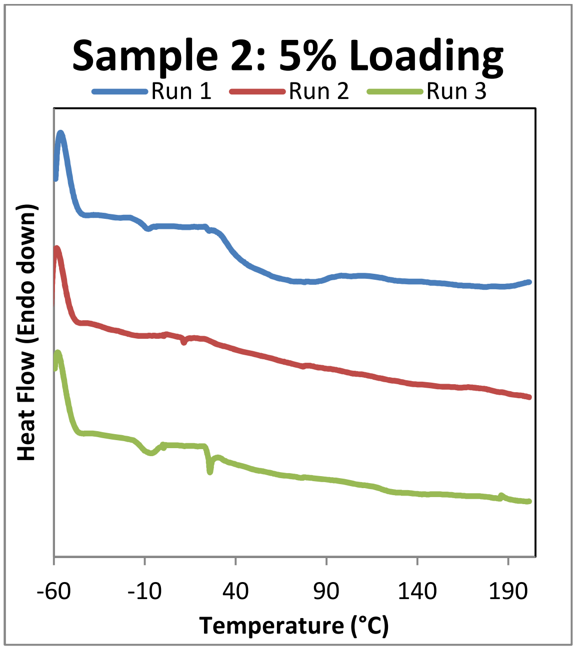

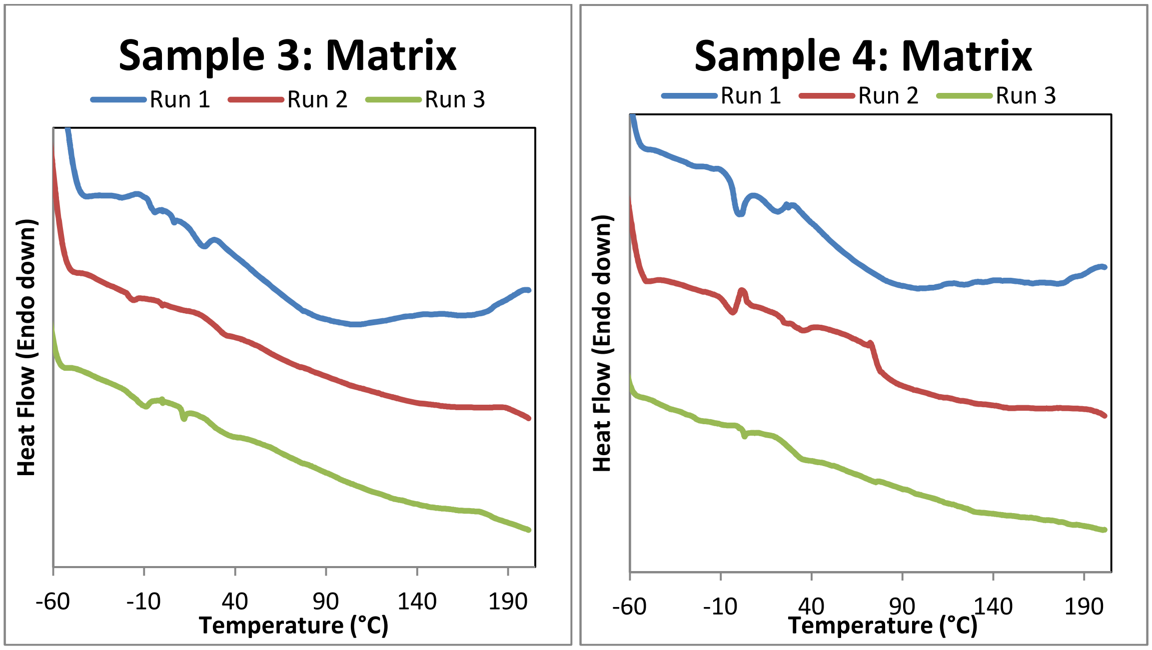

Figure 5.1: Differential scanning calorimetry measurements for samples 1-4.

A similar sample preparation method was followed for two other samples for DSC measurement. Some of the mixture was placed into two DSC aluminum pans. The pans were heated on a hotplate to remove any volatiles, and then transferred to a vacuum oven where it was heated at 120℃. After two hours, the oven was turned off and the sample sat in vacuum overnight. The first sample was immediately measured by DSC after removing it from the vacuum oven. The second sample was also removed from vacuum at the same time. It was measured by DSC once the first sample was finished, two hours later. This is done to reduce exposure to humidity. The starting 5% nanocomposite solution in the vial was much thicker than the solution used for the experiments discussed earlier in this section. Over time, evaporation of solvents/additives occurred, leaving behind a thick slurry of the matrix components. Unfortunately, this results in a different starting state than for the experimental results shown in Figure 5.1. The DSC measurements were carried out with the samples under N_2 atmosphere. At the end of a heating run, the samples were not rapidly cooled but instead measurements were obtained during cooling. Heating and cooling rates of 10℃/min were used. The two samples measured are identified as Sample 5 and Sample 6, in the order that they were measured in.

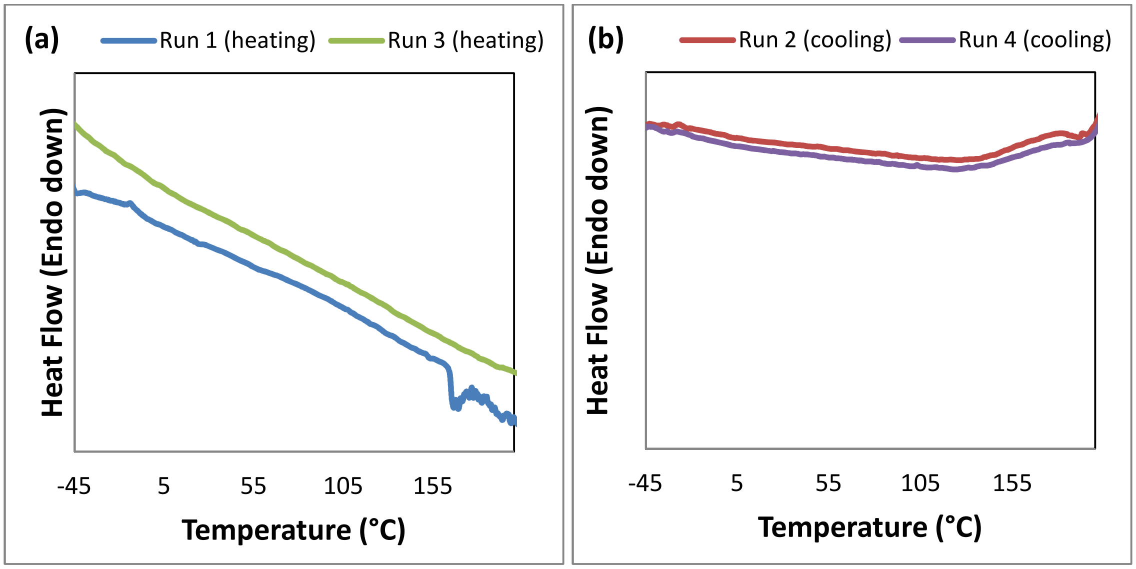

Figure 5.2: DSC results for Sample 5 for a) heating runs and b) cooling runs. The heat flow axis is set to the same range for a) and b).

Sample 5 had four runs collected. The first run was a heating run which was followed by consecutive cooling and heating runs. The first heating run showed a small exotherm at -15℃. Near 160℃, the sample appeared to have undergone a dramatic change. It is possible that some of the more volatile components remained trapped in the matrix, and eventually built up enough pressure for those components to break out of the surrounding polymer. When the sample was heated on the hot plate before measurement, frequent stirring was necessary to help the volatile compounds out. The polymer material would form bubbles, displaying the elastomeric nature of the polymer. The second heating run, run 3, showed no obvious thermal transitions. The two cooling runs were relatively consistent with one another. The measured cooling data is noisier than the heating runs. This may be due to vibrations in the system as liquid nitrogen is pumped in to cool it. A broad endotherm appears at 140℃ for runs 2 and 4. Some weak exotherms appear between -25 and -40℃. Aside from the features discussed, the DSC results for these samples were quite uneventful compared to previous measurements of Samples 1-4. The material may have reached a stable state, where the polymer segments are mixed well. When segment domains exist, there are many thermal responses to consider. Hard and soft segment domains will respond differently as if they were two separate phases in the material. There would also be thermal behaviour which is dependent on the interactions between the two segments. The lack of crystallization and melting events implies that the system is amorphous, and behaves more like a homopolymer.

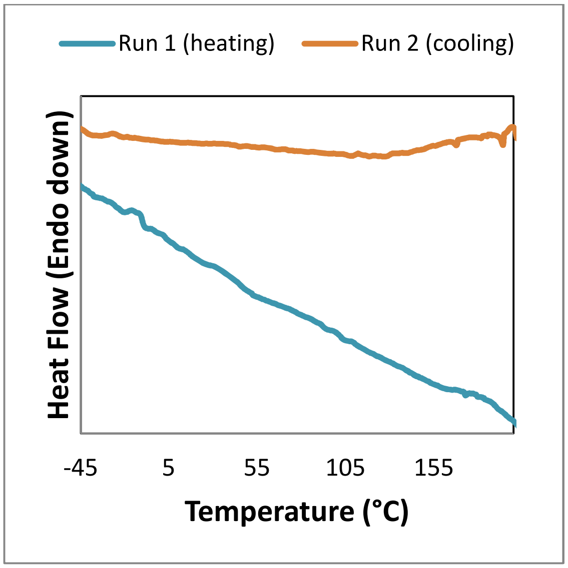

Figure 5.3: DSC results for Sample 6.

Two runs were measured for Sample 6, one heating and one cooling. Similar to Sample 5, a weak exothermic peak at -14℃ is apparent only in the first run, and is not observed in the cooling run. This sample did not experience any significant changes around 160℃. Similar to Sample 5, a broad endotherm in the second run is observed at 140℃.

In summary, despite 6 hours in the vacuum oven to drive off water, the polyurethane matrix still appears to be undergoing conformational changes. The inconsistent temperature and change in enthalpy of the soft segment endotherms demonstrates the environment surrounding the soft segment is changing. A sharp endothermic peak is characteristic of polyurethanes which show domain separation where the soft segments can flow freely until they melt. When the endotherm is hindered, there is good miscibility of segments, and the soft segment becomes trapped inside the hydrogen bonded network of the hard segments. Restricting the motion prevents the transition from occurring. Samples 4 and 5 show signs that the matrix settled into a thermodynamically stable state while water/dispersants slowly evaporated over several months, with some components still trapped inside the matrix. Assuming sample 5 did not have enough time to absorb any moisture from the air prior to measurement, it is possible that the broad endotherm observed earlier in the first run for Samples 1-4 was due to water interactions in the matrix. No discernible relationship between samples with and without nanoparticles could be concluded from these results.

5.3 Thermogravimetric Analysis

To prepare a sample for thermogravimetric analysis, a drop of 5% nanoparticle solution was placed into a heated crucible. The hot plate used to heat the sample was set to 120℃ in order to evaporate the water. The material was stirred frequently to facilitate the process. Once the sample appeared dry, the crucible was placed in a vacuum oven at 110℃ for several hours. The oven was then turned off and the sample remained in the chamber to slowly cool overnight. For data collection, the instrument used was a STA-409 Luxx by Netzsch. Crucibles for TGA were made of Al_2O_3. The sample was heated at 5°/minute with N_2 purge gas.

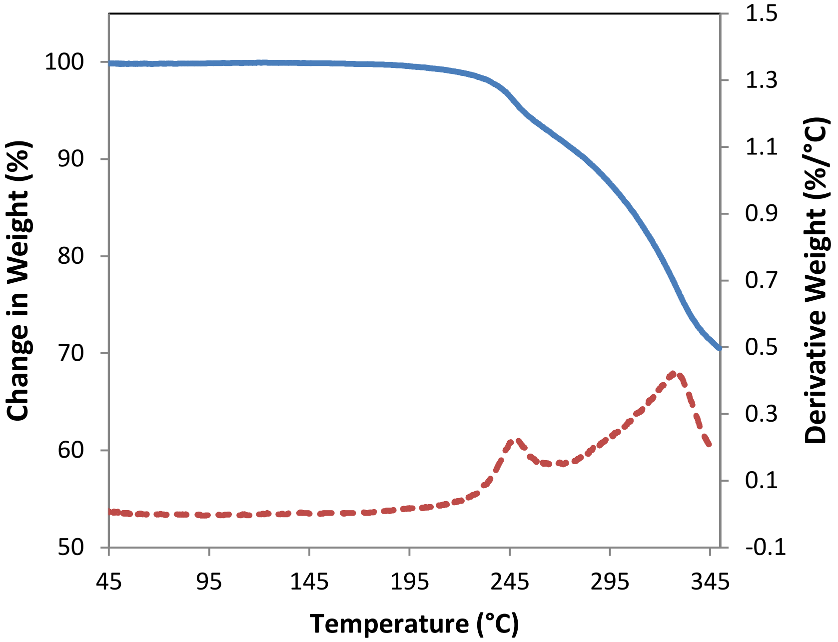

Figure 5.4: Thermogravimetric and differential (DTG) curves of polyurethane nanocomposite material under N_2 atmosphere. Between the onset of degradation and the end of the measurements (345°C), the DTG red dotted pattern indicates that decomposition appears to occur in two steps.

In Figure 5.4, the extrapolated temperature onset (T_{onset}) of mass loss occurred at 238°C. The value for T_{onset} is the initial temperature of system degradation, determined from the intercept of the zero-line (no weight loss) with the tangent from the inflection point of the decomposition step. During the course of the measurement the sample lost 29.5% of its starting mass. The bimodal peaks in the first derivative curve correspond to the temperature at maximum rates of weight loss. Change in weight data was collected up to 350°C. The presence of several peaks is common, depending on the complexity of the degradation process.

T_{onset}	T_{1max} (°C)	T_{2max} (°C)	% Yield (100°C)	% Yield (200°C)	% Yield (300°C)
238	249	327	99.9	99.5	86.3

Table 5.3: Key temperature points and remaining weight fraction values at different temperatures determined from thermogravimetric analysis.

In polyurethane decomposition, the weakest chemical bond is the urethane group [52]. The temperature at which the urethane bond breaks will depend on the constituents surrounding the bond. Several kinetically different routes for urethane group decomposition are possible [52], depending on the chemical nature of the structure. Since polyurethanes vary widely in composition, thermal studies show considerable variation in results. A two-step decomposition similar to the one seen in Figure 5.4 has been observed in several other works [53], [54]. The first onset of decomposition is likely from the dissociation of the urethane bond, due to its lower stability. The second step has been attributed to decomposition of ester groups [55]. Fourier transform infrared spectroscopy on gas emission during these steps has shown carbon dioxide release during the onset of degradation, and butyl ether in the second step, confirming the order of degradation steps [54]. However, the measurement was stopped at 350°C, before full degradation occurred. There may be more degradation modes which occur at higher temperatures. For example, Coutinho *et al.* [53] have found that polyurethanes made with hydroxyl-terminated polybutadiene (HTPB) show three distinct stages, while in the absence of HTPB a two-step degradation occurred.

5.4 Single Wavelength Ellipsometry Monitoring of Glass Transitions

The use of ellipsometry in monitoring glass transitions has become a valuable technique ever since its introduction in 1993 by Beaucage, Composto, and Stein [56]. Physical quantities which can be obtained from ellipsometry, such as index of refraction and film thickness, will vary with temperature, and can be used to profile the glass transition. Several material properties including heat capacity, shear modulus, viscosity, and thermal expansion, show kinks when plotted against temperature. The kinks are a result of sudden changes in the material property when the material transitions between glassy and rubbery states. Measurements of these variables can be monitored to determine the glass transition.

To monitor changes in the nanoparticle films upon heating, a single wavelength ellipsometer was utilized. The angle of incidence was calibrated with a clean silicon wafer prior to each temperature experiment, at a position near 45°. A Linkam heating stage served as the temperature control unit. A series of runs with a particular temperature profile were employed for two different temperatures; 80 and 120℃. For the experiments, spin cast films from a 3:1 dilution of the 5% nanoparticle mixture were prepared.

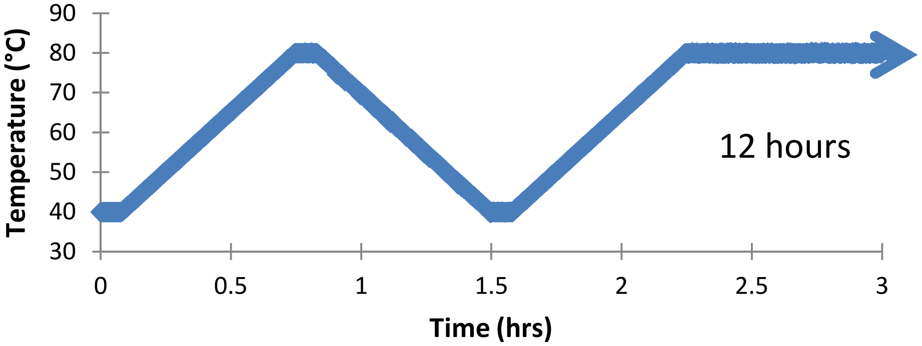

Figure 5.5: Temperature profile used in several runs of the first sample. Sample was exposed to a maximum temperature of 80℃, and annealed at the end of each temperature run.

The first sample was heated according to the profile in Figure 5.5. With the exception of the final step, the temperature was held for 5 minutes at each minimum (40℃) and maximum (80℃) point. The heating and cooling rate between steps was 1℃ per minute. The final heating step was held for 12 hours and returned to room temperature once completed. A total of 14 runs with this profile were done on the sample. Run 10 followed a similar profile except it was left to anneal for 48 hours after it finished its temperature cycle. The computer collecting the data had a tendency to crash during the measurement, particularly near the end of a run. Consequently, some data points are missing. Although some measurements may not have recorded, the linkam temperature unit runs independently of the computer, and therefore all cycles continued to run until completion.

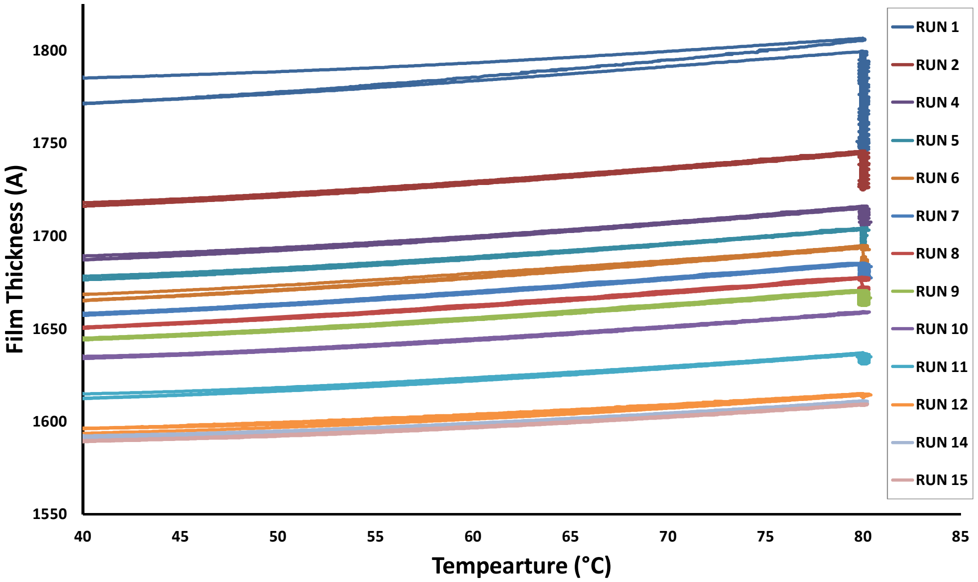

Figure 5.6: Monitoring of coating thickness during several heating and cooling cycles. At the end of each cycle the sample was annealed at 80℃. Run 3 was omitted since the ellipsometer was calibrated incorrectly prior to measurement.

After run 11, the sample was placed in a vacuum oven at 80℃ for six days. Although an effort was made to examine the same sample area when mounted back on the ellipsometer stage, the setup was slightly changed by a previous user and it is expected that a marginally different area was studied for runs 12-14.

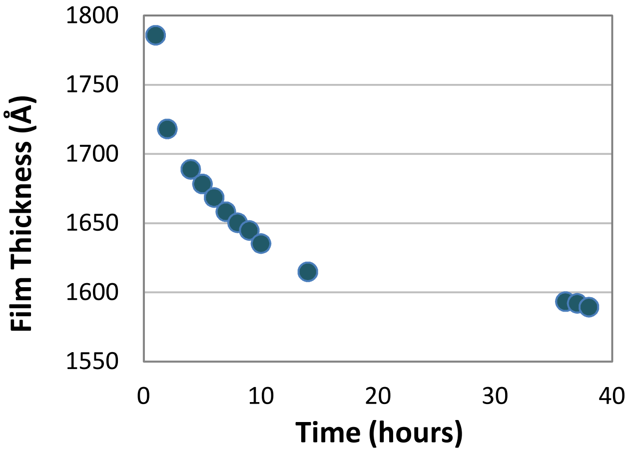

Figure 5.7: Variation of starting thickness with annealing time for temperature cycles reaching a maximum temperature of 80℃.

The starting thickness before each run is presented in Figure 5.7. An overall trend in the data shows that the film is getting thinner with each temperature cycle. After the first run, the thickness decreased by 68nm. If degradation of the polymer to the point of material loss was occurring during the cycles, a continuous depletion would be observed through all the runs until no more material remains. The initial drop is much steeper than the changes observed in the other runs, and the film thickness eventually reaches a stable state. This suggests that the bulk polymer does not go through degradation. The large initial irreversible change can be attributed to relaxation of the polymer matrix. Increasing the temperature of a polymeric system is known to induce or accelerate conformational changes which bring the arrangement into a lower energy state. Another possible explanation for the greater thickness change after the first run is that there is loss of a limiting matrix component, such as water. Dispersing additives in the initial colloidal mixture may also be depleted at this time. With each consecutive run, the magnitude of the change in thickness decreased, providing evidence that the film is approaching equilibrium. Within error, the three runs after the 6 day vacuum oven anneal did not change. Errors such as instrumental drift and errors arising from assumptions applied in the model calculation infer that the 1-3nm observed variation is negligible. The thickness is modeled using the obtained ellipsometric values, assuming that the system is ideal. If the annealing is causing modifications at the surface of the coating, than the values determined for the thickness may drift from the true value.

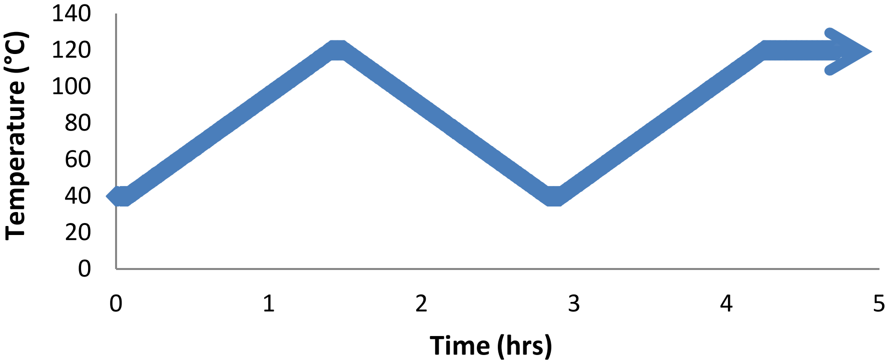

Figure 5.8: Temperature profile used in several runs of the second sample. Sample was exposed to a maximum temperature of 120°C, and annealed at the end of each temperature run.

The second sample was heated according to the temperature profile seen in Figure 5.8. The final annealing step varied between runs, but was typically much longer than the 12 hour hold done for 80°C runs. The ramping rate between steps was 1°C/min with the temperature held for 5 minutes at each step. The time span of the final step anneal for each run can be found below in Table 5.4.

Run #	**1**	**2**	**3**	**4**	**5**	**6**	**7**	**8**
Annealing Time (hrs)	18	18	65	18	45	120*	18	18
Run #	**9**	**10**	**11**	**12**	**13**	**14**	**15**	
Annealing Time (hrs)	113*	18	18	112*	Lost null	18	18	

Table 5.4: Length of anneal at the end of each run. Blue indicates measurements which required a 0.3 neutral density filter to find a null, green indicates the measurements which required a 0.6 neutral density filter, and an asterisk indicates that annealing was done in a vacuum oven. The null for Run 13 was lost early in the measurement and therefore data were omitted from discussion and analysis. The ellipsometer and heating apparatus were stopped and restarted as Run 14 with a stronger neutral density filter.

Longer anneals, indicated in the table, involved removing the sample from the ellipsometer stage and placing them inside a vacuum oven. Markings on the ellipsometer mounting stage were made so that subsequent runs were collected at a similar location on the sample. During the setup for run 10, after a long 112 hour anneal, the null could not be detected. If the beam leaving the polarizer has a high intensity it saturates the detector, making it impossible to find a null. To detect the null, a neutral density filter with an optical density of 0.3 was placed before the detector. The filter remained in place for the data collection. After another long anneal of 113 hours, finding the null for run 14 was found challenging even with the filter present. A stronger filter with 0.6 optical density was used for the final temperature runs. The requirement to use a filter to find null implies the sample is straying from an ideal system.

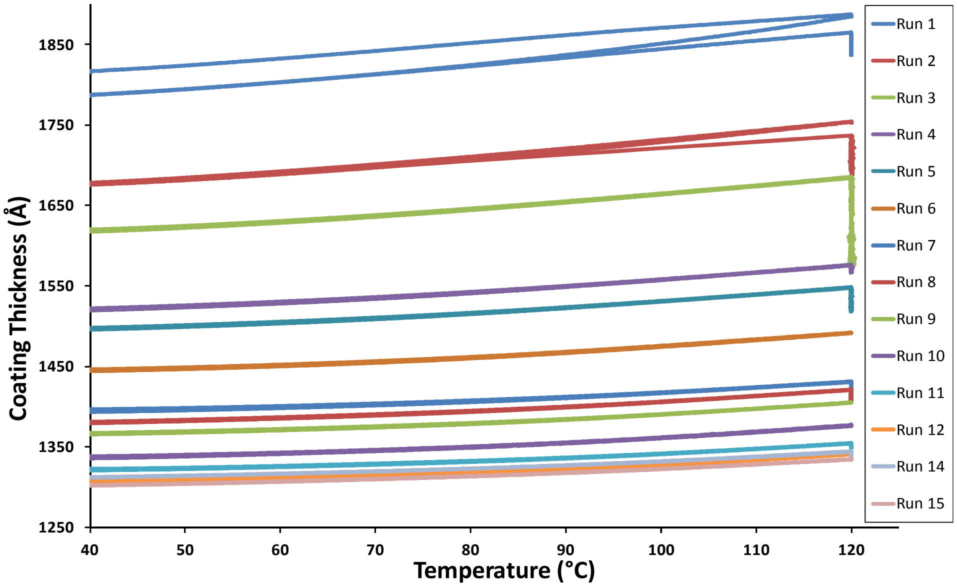

Figure 5.9: Monitoring of coating thickness after several annealing events. Annealing was done at 120℃. Run 13 is omitted since the null was outside the detection limit, and the run had to be restarted as Run 14 with a neutral density filter present.

To investigate what physical changes are causing the non-idealities upon heating, a sample cast on a glass substrate, with similar coating thickness as the experiment discussed in this section, followed a parallel 120℃ annealing procedure. The sample was measured using UV-Vis spectroscopy before, midway through, and after annealing. A coating cast on a cleaved silicon wafer substrate also followed the same procedure. Measurements using AFM and TEM were done during the different stages of annealing to monitor changes in surface texturing and/or particle distribution.

5.5 Thermal Effect on Nanoparticle Films as Examined by TEM

Three 5% nanoparticle films were prepared from an 8:1 dilution of the original mixture. A 0.2 μm filter was in place on the syringe when the mixture was dropped on the substrate surface. The films were spun on clean, freshly cleaved mica and then floated into an ultra pure water bath. The resulting films were between 50-80nm in thickness. To investigate the effects of heating on the nanoparticle films, a control and two different heat treatments were done. The thermal treatments for each sample were carried through to complement the heat experiments discussed previously in Section 5.4, in order to investigate if any change in nanoparticle distribution occurs in the nanocomposite coating. If heating induces aggregation or segregation of particles, the coating's index of refraction determined by ellipsometry will be influenced by the change. In particular, the effective medium will lose validity if the concentration and size of aggregates becomes high, resulting in an index of refraction and a thickness with a large error. Segregation of nanoparticles toward either interface would create a graded system, and if not modeled properly would also result in misleading indices of refraction and thicknesses. Since the experiment discussed here involves TEM imaging through the thickness of the film, inferring anything about interface segregation of nanoparticles is not feasible due to lacking depth field. Nanoparticle segregation will be discussed in Section 5.6. This section focuses on monitoring changes in aggregates.

As a control, an unheated sample was included in the analysis. The second sample was heated at 120℃ on a Linkam heating stage. A temperature of 190℃ was chosen for the third sample to observe nanoparticle behaviour beyond the glass transition temperature. After the one hour anneal, the two heated samples were rapidly cooled to room temperature and floated onto TEM grids for examination. The control sample was also floated.

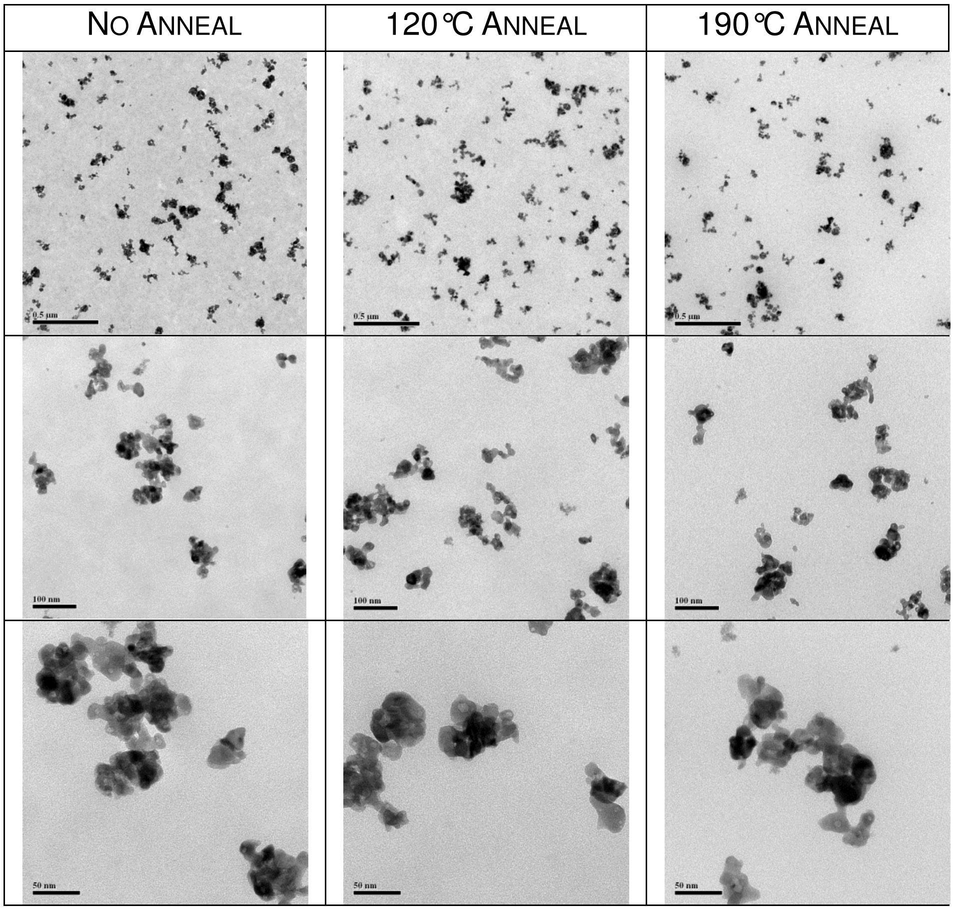

Figure 5.10: Comparison of 5% ITO nanocomposites after no treatment, annealed at 120℃, and annealed at 190℃. Samples were examined at three magnifications.

In the above figure, no apparent differences in nanoparticle distribution are observed. The original spun films had variations in thickness of up to 30 nm. Since the images are looking through the top of the film, and don't provide any depth information, the density of particles would appear higher for thicker films.

From the lower magnification images, it appears as though the 190℃ annealed sample has a lower NP density. However, since no increase in aggregate size is evident, it is likely a consequence of film thickness. Aside from subtle differences in the apparent density, a random distribution of nanoparticles and clusters of similar size are observed in all three films. Single, or near single, ITO particles are rare but can be identified in all three samples. Cross-sectional TEM imaging will determine if migration of the nanoparticles towards either interface occurs when the films are annealed.

5.6 TEM Imaging of Annealed and Microtomed Nanoparticle Films

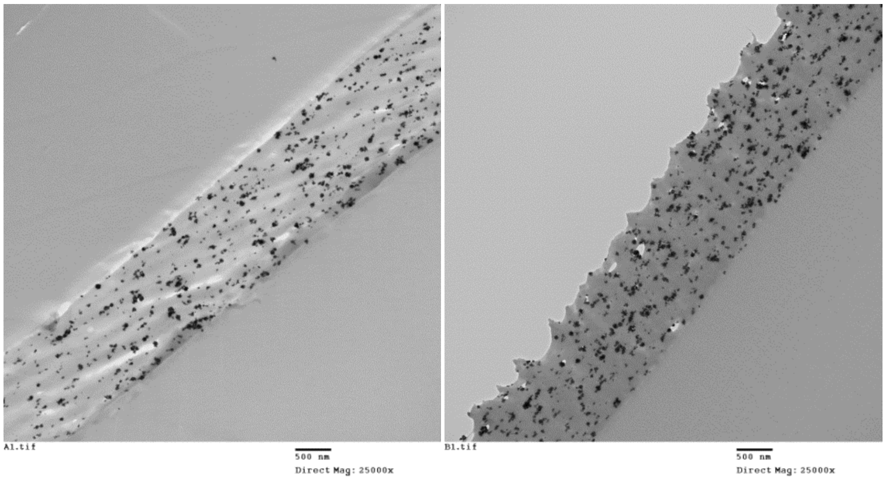

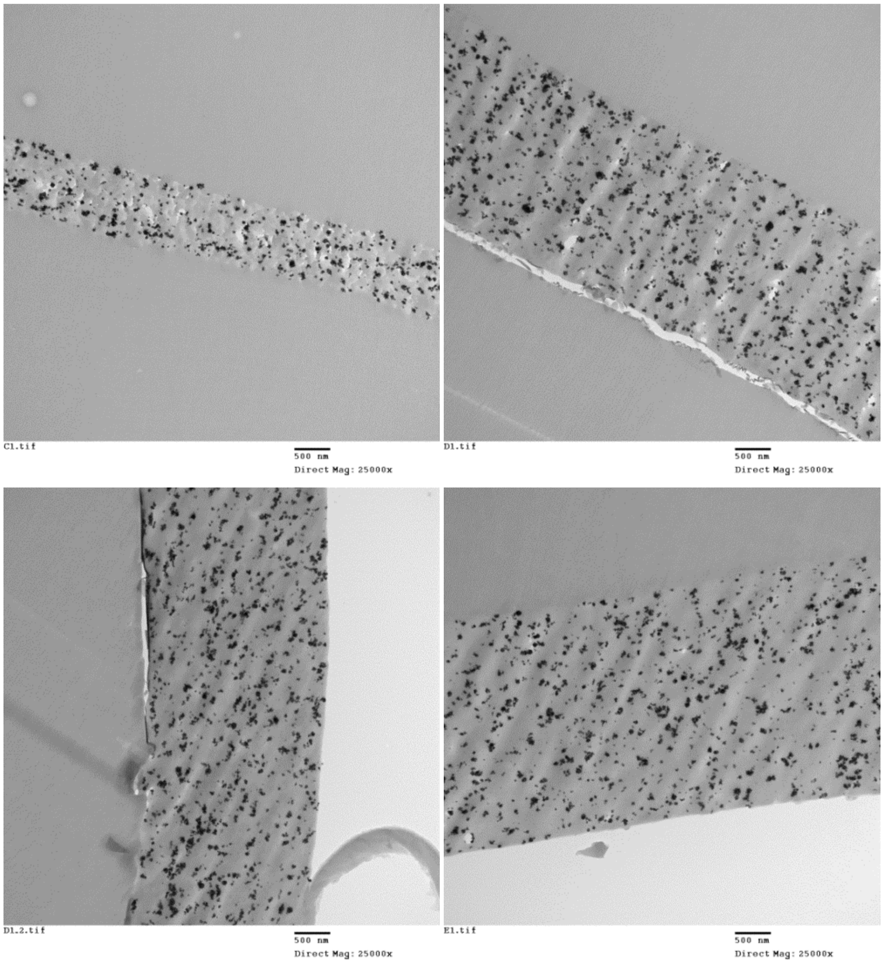

Figure 5.11: Cross-sectional TEM images of annealed nanocomposites

Five films were prepared to determine if the nanoparticles would segregate towards either interface when heated. The first sample, A, was held at 70°C for 4 days, representing the most realistic operating conditions if applied to a solar module. Higher temperatures were tested to observe nanoparticle behavior when temperatures approach and surpass any matrix glass transitions. When the polymer matrix rearranges into a lower energy state, nanoparticles may be driven out towards the film-substrate or film-ambient boundaries. The heat treatment for samples B-E were: 120℃ for 3 days, 180℃ for 4 days, 150℃ for 3 days, and 110℃ for 3 days, respectively.

Preparation of the films for microtoming and examination with TEM followed the same procedure as described in Section 5.4. Due to difficulty in handling the very small segments, wrinkling, tearing, and poor adherence to the polystyrene support can be observed. Despite any imperfections in the samples, information on the nanoparticle distribution can still be extracted from the TEM images. As in previously observed microtomed samples, the visible film edges in the figures correspond to either the ambient or substrate interface of the original film. Since the film segments were so delicate and small, the orientation was difficult to track, and therefore, the visible film edges can't be distinguished with confidence. The uniform grey areas in the figures correspond to the polystyrene film support. The nanoparticles are observed as dark specks. Brighter areas between the film and polystyrene are voids, indicating the poor adherence of the two materials.

The first noticeable difference between the five samples is the variation in film thickness. Sample C was annealed at the highest temperature, 180℃, and shows to be the thinnest segment. The starting films were prepared with similar thicknesses, with variation within a few tens of nanometers. Comparing a thickness of about 920nm for Sample C to a thickness of about 1.5µm for Sample A shows a significant change after the annealing treatment. Two possible explanations for changes in thickness can be formulated. Firstly, if film degradation occurs, the film would lose material when subjected to sufficiently high temperatures. Another possibility is that annealing causes the matrix to contract as it conforms to a more thermodynamically stable state.

5.7 Atomic Force Microscopy

The same sample measured by ellipsometry which followed the annealing profile described in Figure 5.8 and Table 5.4 was measured by AFM before, mid-way through, and after the annealing process. During the ellipsometry measurement, the null became progressively more difficult to find. The use of neutral density filters was required to continue with the measurement. As mentioned in Section 5.4, this occurs when the coating drifts away from ideal homogeneous layers. The AFM measurements were done to monitor changes at different stages in the annealing process. Prior to the first annealing run, the coating surface was measured. With the AFM instrument it was difficult to consistently measure the same location on the sample. Subsequent runs were within a few millimeters from the first measurement. The measurement mid-way through the annealing cycles was done after Run 6 on the ellipsometer. The final AFM measurement was done after Run 15 on the ellipsometer.

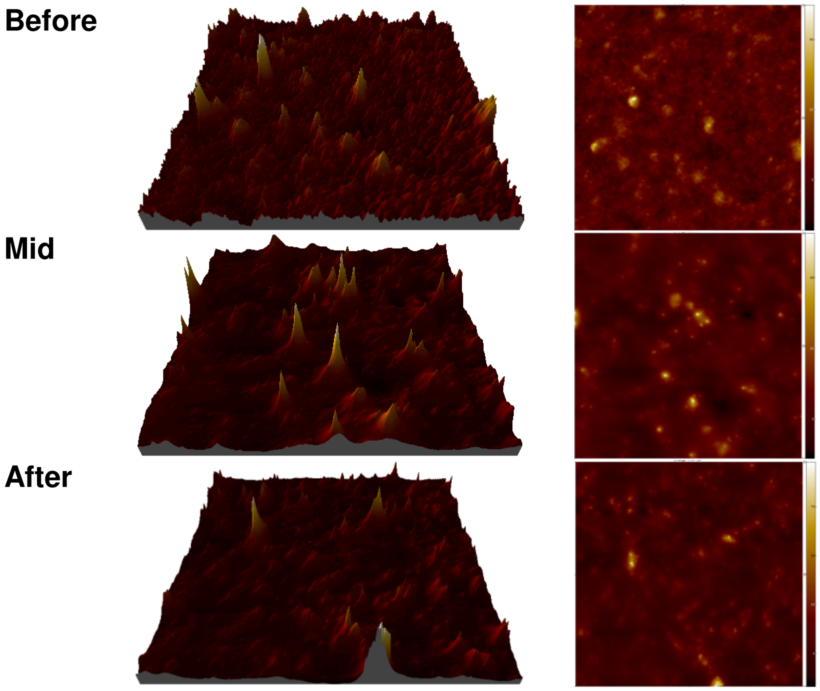

Figure 5.12: AFM images of a sample before, mid-way through, and after annealing. A scan size of 5µm was measured for all images in this figure.

Comparison of the sample at different stages in the annealing process reveals some changes in the texturing. In Figure 5.12, the initial measurement shows a rough surface with a few distinct peaks which are likely nanoparticles near or at the surface of the coating. The rough surface starts off with many small sharp peaks. After annealing, these smaller peaks smooth out into broad peaks and valleys. A significant difference is not observed between the measurements midway through and after annealing. It appears that the final measurement consists of fewer large peaks. However, it may be that a region of the coating with lower particle density was probed. Several areas were examined at each of the three stages and the average surface roughness values are listed below in Table 5.5.

	BEFORE	**(nm)**	**MID**	**(nm)**	**AFTER**	**(nm)**
Range (μm)	**RMS (avg)**	**RA (avg)**	**RMS (avg)**	**RA (avg)**	**RMS (avg)**	**RA (avg)**
2	3.6	2.8	3.6	2.8	6.9	4.8
5	6.0	4.1	4.7	3.3	6.6	4.5
5	4.8	3.6	6.2	4.1	6.5	4.6
30	5.0	3.5	5.0	3.5	7.9	5.4
Avg.	4.9	3.5	4.9	3.4	7.0	4.8
Std. Dev.	0.8	0.4	1.3	0.6	0.7	0.4

Table 5.5: Average surface roughness values before, mid-way through, and after annealing at 120℃.

Four regions on the sample were examined at each stage during the annealing process. The average roughness before and mid-way through the anneal (7 days) was the same within a standard deviation. Earlier qualitative observations of the 2D and 3D AFM revealed that small sharp fluctuations in the background became broader after annealing. However, the material coming up and creating the broader peaks are also creating valleys. Consequently, the average surface fluctuation does not change after 7 days of annealing despite the observable changes on the surface in Figure 5.12. After all the annealing runs (26 days), the coating surface became rougher. Since the coating became thinner throughout the annealing procedure, it may be that large agglomerates began to perturb the surface.

The difficulty in finding null with the ellipsometer during sample annealing can be explained by modifications occurring on the surface. Small features, considerably smaller than the wavelength of the laser probe used, can be treated as components of an effective medium, consisting of the nanocomposite and void. Assuming the EMA layer is consistent across the area of the laser beam, null would not be affected. Non-uniformities on a larger scale would cause the null to drift from ideal. The increase in surface roughness may be a result from large, broad features that inconsistently appear, such as agglomerates, or from thickness non-uniformities that developed in the coating as it was heated. To test if agglomerates are causing the surface roughness to increase due to thickness constraints of the film, two thicker films were examined. The results and discussion are found in the following section.

5.8 Atomic Force Microscopy of Annealed Thicker Films

In Chapter 4, it was observed by SEM and TEM that the sizes of some agglomerates were near 100nm long. The final thicknesses of the films annealed during single wavelength ellipsometry measurements in Section 5.4 were 120-160nm thick. With agglomerates approaching sizes that are similar to the film thickness, it would be expected that the surface of the film would change after annealing. Whether the reduction in thickness is due to the polymer contracting or decomposing when heated, the agglomerates remain in the system. With nowhere else to go, they may become exposed at the surface, increasing the observed roughness. To determine whether the strong features found in Section 5.7 are only due to space constraints in the thin films, two thicker samples were tested by AFM. The samples were prepared from as received solutions of 5% nanoparticle loading. Previous samples prepared from the as received solutions were determined by VASE to be near 2μm in thickness. One film was stored at room temperature, while the other was placed in a vacuum oven at 120℃ for 4 days.

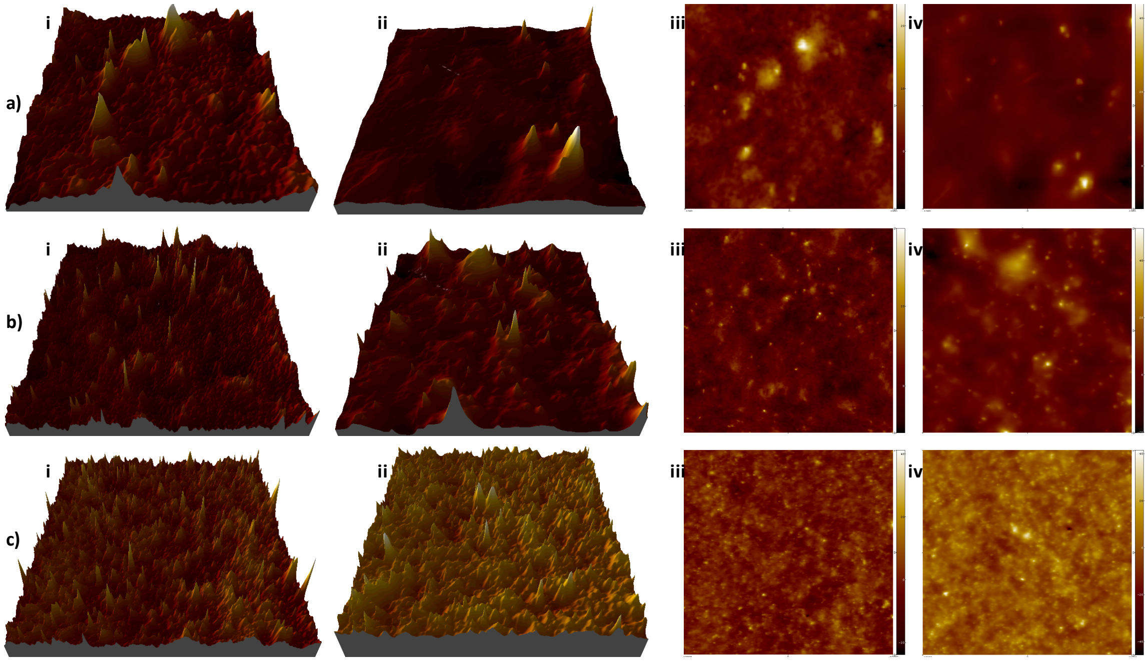

Figure 5.13: AFM images of thicker films before (i, iii) and after (ii, iv) annealing. Images displayed in 3D (i, ii) and 2D (iii, iv). Scan sizes were 2, 5, and 20μm in a), b), and c) respectively.

Three different scan sizes, and several locations on the sample were examined. In Figure 5.13 there are some notable differences between the room temperature sample and the annealed sample. First, the main background surface roughness appears much smoother for the annealed sample. This is best observed in the 2μm scan, where small spikes found initially disappeared once the sample was annealed. Second, the strong peaks found initially in the sample increased in width after annealing. This is best observed in the 20μm scan since a larger area is sampled. During annealing, the film has enough energy to undergo conformational changes. The tall thin spikes have large surface to volume ratios, leading to high surface energy. Broadening of the peaks, which are likely nanoparticles near the coating surface, occurs from either material traveling up and around the sharp features, or the sharp features flattening down. The RMS and average values integrated from the data reveal an increase in magnitude after annealing, supporting that the material creeps up to form the broad surface features. Resulting surface roughness measurements are found in Table 5.6.

No Annealing			After Annealing		
Range (µm)	**RMS (avg) (nm)**	**RA (avg) (nm)**	**Range (µm)**	**RMS (avg) (nm)**	**RA (avg) (nm)**
40	3.59	2.72	5	6.44	4.60
2	3.17	2.23	20	5.43	4.15
5	3.35	2.53	2	4.05	2.64
5	3.59	2.56	5	4.03	3.13

Table 5.6: Surface roughness values for a sample that has not been annealed, and one which was annealed in a vacuum oven for 4 days at 120℃. The average root mean squared (RMS) and arithmetic average (RA) surface roughness values are listed for each scan area measured.

Testing thicker films revealed that the increase in surface roughness after annealing is also observed in thicker films. The roughness is expected to result from the minimization of surface energy as opposed to an increase of nanoparticles and agglomerates at the surface. Since particle segregation after annealing was not evident by TEM in Section 5.6, and size constraints are not present in the two thicker films examined in this section, the increased annealing roughness is due to flow of polymer and particles already near the surface.

Chapter 6: Conclusion

Nanocomposite coatings comprised of commercial grade polyurethane, ITO nanoparticles, and dispersing agents (ethylene glycol and carboxylate-PEG) were prepared by spin casting water-based solutions onto clean silicon and glass substrates. Dry ITO nanoparticle powder and solutions with 0%, 1%, 3%, 5%, 10%, 15%, and 20% nanoparticle loading by weight were provided by Hy-Power Coatings Limited©. To determine the optical, physical, and thermal properties, the coatings were characterized by ellipsometry, UV-Vis spectroscopy, SEM, TEM, EDX, AFM, DSC, and TGA.

The dielectric functions of the nanocomposite coatings were modeled from VASE measurements. Modeling began with the characterization of pristine coatings. Optical functions for the silicon substrate and native oxide layers were obtained from the built-in database in the CompleteEASE software. A series of 13 samples with varying thicknesses were studied. The optical properties of the coating for all 13 samples were coupled to a single common Cauchy function in a multi-sample analysis. Film thickness was fit independently for each sample. A thickness non-uniformity parameter was included in the model. The resulting parameters are A=1.495, B=0.00468nm^2, and C=0.0000884nm^4. The Cauchy relation was then applied to systems with ITO inclusions.

Modeling of the nanocomposite system was accomplished by applying the effective medium approximation. EMA modeling began with a series of 5% ITO nanocomposite samples. Several approaches were taken to reduce the number of free variables: (1) Determined surface roughness of samples using AFM, (2) Coupled ITO volume percent and optical function for the 5% samples series, (3) Constrained the Cauchy function for the polymer matrix, and finally (4) limited the spectral range to 370-650nm, where the extinction coefficient for ITO can be assumed to be zero. In the region where ITO is transparent, the index of refraction may be modeled using the Cauchy function. Once the model converged, the calculated volume percent and film thicknesses were fixed, and the spectral range was expanded to include all the data. The ITO optical function was parameterized from the Cauchy dispersion into two Lorentz oscillators, located at the low infrared and high ultraviolet regions. The final fit determined the energy and amplitude of the Lorentz oscillators, and consequently the ITO dispersions for the full range. The EMA function for the 5% ITO nanocomposites was calculated from the combination of the matrix and ITO dispersions.

The EMA model which was determined using the 5% ITO sample series was individually applied to the 1%, 3%, 10%, 15%, and 20% loaded samples. In these cases, the only fit variables were the coating thicknesses and the coupled volume percent. The MSE indicated the quality of fit for each nanoparticle loading. The MSE increased with increasing nanoparticle loading. At higher loadings, the system became difficult to model using an EMA layer due to the increased density of agglomerates.

UV-Vis spectroscopy on a series of coatings casted on glass cover slips was performed to determine the affect of nanoparticle loading on the transmittance. All coatings from 0-20% nanoparticle loading showed greater than 90% transparency in the visible range. With the coating present, the onset of absorption in the ultraviolet range occurred at 400nm, while a clean glass cover slip had absorption at 300nm. Higher loadings showed lower transmittance throughout the spectra. However, the ultraviolet regions were the most affected by nanoparticle density. In the visible range, transmittance demonstrated little sensitivity. The near-infrared region also showed increased shielding with nanoparticle loading. The addition of nanoparticles successfully maintained high transparency in the visible range, and displayed the potential for tunable UV/IR-shielding.

Imaging by SEM and TEM shows that the majority of the particles exist as agglomerates. Sizes of the agglomerates typically had dimensions between 30-250nm. Single nanoparticles were characteristically 10-20nm wide, with an oblong appearance. The distribution of nanoparticles in the coating appeared random, with no apparent segregation toward film-air or film-substrate interfaces. Several different features were observed by TEM of the nanoparticle powder. The crystalline nature of the particles was confirmed with the presence of diffraction fringes. Small circular structures appeared near particles and agglomerates. It could not be discerned whether these were features on the surface or inside the particle. Amorphous regions and connective material between particles in the agglomerates were also observed. Imaging of samples annealed at 80, 120, and 190°C showed no evidence of changes in particle distribution. Increase in agglomeration or particle segregation were not apparent.

A bulk pressed pellet was examined by EDX. The bulk average atomic fraction of tin in ITO was 6.5%. Nanoparticle clusters suspended on a carbon supported copper grid were also examined and the average tin content was 8.4%. The composition was not uniform between clusters. Surface roughness of samples with 0%, 1%, 3%, 5%, 10%, and 15% nanoparticle loading were measured with AFM. Values were constrained in the VASE model. The average and RMS roughness of the pristine coating were 24Å and 31Å respectively. As the nanoparticle content increased, the surface became rougher, with the exception of the 20% sample which had roughness values comparable to the 5% sample. It is unclear whether high nanoparticle loadings begin to improve surface roughness or if some other variable is influencing the surface. Spin casting parameters such as angular velocity and solution concentration would stimulate changes in the casting dynamics, and thus change the surface. Further sampling and testing is required to draw further conclusions.

Thermal stability of the coatings was examined using DSC, TGA, ellipsometry, and AFM. Initial measurements of 4 samples by DSC showed a broad transition between 45-85°C in the first measurement run. This transition faded with consecutive runs. Two new samples were prepared several months later from a starting solution that had lost most of its water. After sitting in the vacuum oven prior to measurement, the samples were quickly measured by DSC to ensure the samples are not exposed to moisture prior to measurement. The broad endotherm was not present for samples 5 and 6. Since the starting solution was not consistent, it is not certain whether the broad endotherm is due to the hygroscopic nature of the material, or if thermodynamic changes occurred as the water evaporated from the vile. Between DSC runs in samples 1-4, the presence of crystallization exotherms and melt endotherms showed inconsistent behaviour. The matrix was constantly undergoing changes during the measurement. In polyurethanes, transitions occurring at lower temperatures are due to changes in the amorphous soft segment. From DSC, it was estimated that the soft segment glass transition occurred somewhere in the range of -15 to 30℃. Crystallization and melting was atypical, and there is more evidence supporting that the soft segment and hard segment showed good miscibility. With most transitions occurring with small changes in enthalpy, the system appeared to behave closer to a homopolymer as opposed to a system with segmental domain separation. The erratic transitions may occur due to interactions of dispersing agents with the system. One known agent present in the matrix is ethylene glycol, which has melting and boiling points greatly dependent on its chemical environment. TGA measurements determined the onset of mass loss occurred at 238℃. The degradation process had two steps up to the measured 350℃. Multi-step decomposition is common for polyurethanes, with the dissociation of different bonds requiring different amounts of energy. Due to lower stability, the urethane bond is often the first degradation step.

Monitoring thickness changes in the coating during annealing was performed by nulling ellipsometry. Samples were cycled through heating and cooling runs, with long annealing times at the end of each cycle. The thickness of the coating decreased when heated to 80℃ or 120℃. Before it reached equilibrium after the 80℃ anneal, the thickness of the film decreased to 89% of its initial thickness. This is only a 50nm difference. After the 120℃ anneal, the system equilibrated to 72% of its starting thickness, or a loss of 20nm. These changes occurred after several weeks of thermal treatment and are not significant. After several long anneals, the samples became difficult to null on the ellipsometer, evidence that the coating is straying from an ideal, uniform film. Monitoring the surface before, mid-way through, and after the annealing runs at

120℃ provided incite on the changes occurring. Initially the same is rough with many small sharp features. After some annealing, the small features became broader, with average surface roughness remaining the same, 3.5nm. After several weeks of annealing, the surface had many large peaks, resulting in a larger roughness of 5nm. A test on thicker films, approximately 2μm thick, was performed to see if agglomerates were affecting the surface as the coating became thinner. The thicker films also showed similar increases in the roughness.

The optical, physical, and thermal testing presented in this work has demonstrated the great potential of the coating for application on solar panels. The UV/IR-shielding can be tuned by manipulating the density of nanoparticles and thickness of the coating, while maintaining high transparency in the visible spectral range. Although nanoparticle agglomerates were formed during synthesis, the dispersion of these agglomerates is random in the coating. Some single particles have been successfully synthesized and dispersed in the matrix. Surface roughness was on the order of a few nanometers, and may actually enhance the transmittance as it acts as a graded layer for the path of light. The matrix appeared dynamic during all thermal tests, however the ITO component remained randomly distributed with no apparent segregation. In addition, no degradation of the matrix occurs within expected operating conditions.

Work Cited

[1] E. Boysen, N. C. Muir, D. Dudley, and C. Peterson, *Nanotechnology For Dummies*, 2nd ed. For Dummies, 2011, p. 8.

[2] L. Li, M. Fan, R. C. Brown, J. (Hans) Van Leeuwen, J. Wang, W. Wang, Y. Song, and P. Zhang, “Synthesis, Properties, and Environmental Applications of Nanoscale Iron-Based Materials: A Review,” *Critical Reviews in Environmental Science and Technology*, vol. 36, no. 5, pp. 405–431, Oct. 2006.

[3] P. Alivisatos, “The use of nanocrystals in biological detection.,” *Nature biotechnology*, vol. 22, no. 1, pp. 47–52, Jan. 2004.

[4] G. L. Allen, R. a. Bayles, W. W. Gile, and W. a. Jesser, “Small particle melting of pure metals,” *Thin Solid Films*, vol. 144, no. 2, pp. 297–308, Nov. 1986.

[5] J. P. Koppes, A. R. Muza, E. a Stach, and C. H. Handwerker, “Size-dependent melting properties of small tin particles: nanocalorimetric measurements,” *Physical review letters*, vol. 104, no. 18, p. 189601, May 2010.

[6] a N. Goldstein, C. M. Echer, and a P. Alivisatos, “Melting in semiconductor nanocrystals.,” *Science (New York, N.Y.)*, vol. 256, no. 5062, pp. 1425–7, Jun. 1992.

[7] H. Althues, J. Henle, and S. Kaskel, “Functional inorganic nanofillers for transparent polymers.,” *Chemical Society reviews*, vol. 36, no. 9, pp. 1454–65, Sep. 2007.

[8] M. Niederberger, G. Garnweitner, F. Krumeich, R. Nesper, H. Cölfen, and M. Antonietti, “Tailoring the Surface and Solubility Properties of Nanocrystalline Titania by a Nonaqueous In Situ Functionalization Process,” *Chemistry of Materials*, vol. 16, no. 7, pp. 1202–1208, Apr. 2004.

[9] M. Haridas, S. Srivastava, and J. K. Basu, “Tunable variation of optical properties of polymer capped gold nanoparticles,” *The European Physical Journal D*, vol. 49, no. 1, pp. 93–100, Jul. 2008.

[10] K. Haraguchi and T. Takehisa, “Nanocomposite Hydrogels: A Unique Organic–Inorganic Network Structure with Extraordinary Mechanical, Optical, and Swelling/De-swelling Properties,” *Advanced Materials*, vol. 14, no. 16, p. 1120, Aug. 2002.

[11] H.-C. Kuan, C.-C. M. Ma, W.-P. Chang, S.-M. Yuen, H.-H. Wu, and T.-M. Lee, “Synthesis, thermal, mechanical and rheological properties of multiwall carbon nanotube/waterborne polyurethane nanocomposite,” *Composites Science and Technology*, vol. 65, no. 11–12, pp. 1703–1710, 2005.

[12] J.-H. Yeun, G.-S. Bang, B. J. Park, S. K. Ham, and J.-H. Chang, “Poly(vinyl alcohol) nanocomposite films: Thermooptical properties, morphology, and gas permeability,” *Journal of Applied Polymer Science*, vol. 101, no. 1, pp. 591–596, Jul. 2006.

[13] S. Singha and M. Thomas, “Dielectric properties of epoxy nanocomposites,” *IEEE Transactions on Dielectrics and Electrical Insulation*, vol. 15, no. 1, pp. 12–23, 2008.

[14] S. Li, M. Meng Lin, M. S. Toprak, D. K. Kim, and M. Muhammed, “Nanocomposites of polymer and inorganic nanoparticles for optical and magnetic applications.,” *Nano reviews*, vol. 1, pp. 1–19, Jan. 2010.

[15] Y.-Q. Li, S.-Y. Fu, and Y.-W. Mai, “Preparation and characterization of transparent ZnO/epoxy nanocomposites with high-UV shielding efficiency,” *Polymer*, vol. 47, no. 6, pp. 2127–2132, Mar. 2006.

[16] Y. Kojima, A. Usuki, M. Kawasumi, A. Okada, T. Kurauchi, and O. Kamigaito, “Synthesis of nylon 6–clay hybrid by montmorillonite intercalated with ε-caprolactam,” *Journal of Polymer Science Part A: Polymer Chemistry*, vol. 31, no. 4, pp. 983–986, Mar. 1993.

[17] Y. Yang, Z. Zhu, J. Yin, X. Wang, and Z. Qi, “Preparation and properties of hybrids of organo-soluble polyimide and montmorillonite with various chemical surface modification methods,” *Polymer*, vol. 40, no. 15, pp. 4407–4414, Jul. 1999.

[18] V. Kochergin, V. Zaporojtchenko, H. Takele, F. Faupel, and H. Fo□ll, “Improved effective medium approach: Application to metal nanocomposites,” *Journal of Applied Physics*, vol. 101, no. 2, p. 024302, 2007.

[19] U.S. Environmental Protection Agency, “Air Emission Sources,” 2013. [Online]. Available: http://www.epa.gov/cgi-bin/broker?_service=data&_program=dataprog.national_2.sas&_debug=0&sector=Fuel Combustion&pol=SO2&polchoice=SO2. [Accessed: 20-Mar-2013].

[20] U.S. Energy Information Administration, “International Energy Statistics,” 2010. .

[21] R. A. Rohde, “Solar Radiation Spectrum,” *Global Warming Art*, 2007. [Online]. Available: http://www.globalwarmingart.com/wiki/File:Solar_Spectrum_png. [Accessed: 15-Mar-2013].

[22] M. a. Green, “General temperature dependence of solar cell performance and implications for device modelling,” *Progress in Photovoltaics: Research and Applications*, vol. 11, no. 5, pp. 333–340, Aug. 2003.

[23] “New SunPower E20 Series: the world’s first 20 percent efficiency solar panel,” 2012.

[24] G. Makrides, B. Zinsser, G. E. Georghiou, M. Schubert, and J. H. Werner, “Temperature behaviour of different photovoltaic systems installed in Cyprus and Germany,” *Solar Energy Materials and Solar Cells*, vol. 93, no. 6–7, pp. 1095–1099, Jun. 2009.

[25] N. Félidj, J. Aubard, G. Lévi, J. Krenn, M. Salerno, G. Schider, B. Lamprecht, a. Leitner, and F. Aussenegg, “Controlling the optical response of regular arrays of gold particles for surface-enhanced Raman scattering,” *Physical Review B*, vol. 65, no. 7, p. 075419, Feb. 2002.

[26] H. Althues, J. Henle, and S. Kaskel, “Functional inorganic nanofillers for transparent polymers.,” *Chemical Society reviews*, vol. 36, no. 9, pp. 1454–65, Sep. 2007.

[27] P. Tao, A. Viswanath, L. S. Schadler, B. C. Benicewicz, and R. W. Siegel, “Preparation and optical properties of indium tin oxide/epoxy nanocomposites with polyglycidyl methacrylate grafted nanoparticles.,” *ACS applied materials & interfaces*, vol. 3, no. 9, pp. 3638–45, Sep. 2011.

[28] H. Fujiwara, *Spectroscopic Ellipsometry*. Chichester, UK: John Wiley & Sons, Ltd, 2007.

[29] H. Chessin, W. C. Hamilton, and B. Post, “Position and thermal parameters of oxygen atoms in calcite,” *Acta Crystallographica*, vol. 18, no. 4, pp. 689–693, Apr. 1965.

[30] F. L. Pedrotti and L. S. Pedrotti, *Introduction to Optics*, 2nd ed. Prentice-Hall, Inc., 1993.

[31] R. W. Collins, “Automatic rotating element ellipsometers: Calibration, operation, and real-time applications,” *Review of Scientific Instruments*, vol. 61, no. 8, p. 2029, 1990.

[32] W. Sellmeier, “Zur Erklärung der abnormen Farbenfolge im Spectrum einiger Substanzen,” *Annalen der Physik und Chemie*, vol. 219, no. 6, pp. 272–282, 1871.

[33] D. K. Chattopadhyay and K. V. S. N. Raju, “Structural engineering of polyurethane coatings for high performance applications,” *Progress in Polymer Science*, vol. 32, no. 3, pp. 352–418, Mar. 2007.

[34] B. Hartmann, J. V. Duffy, G. F. Lee, and E. Balizer, “Thermal and dynamic mechanical properties of polyurethaneureas,” *Journal of Applied Polymer Science*, vol. 35, no. 7, pp. 1829–1852, May 1988.

[35] W. Chen and S. Schlick, “Study of phase separation in polyurethanes using paramagnetic labels: effect of soft-segment molecular weight and temperature,” *Polymer*, vol. 31, no. 2, pp. 308–314, Feb. 1990.

[36] J. L. Stanford, R. H. Still, and R. N. Wilkinson, “Effects of soft segment prepolymer functionality on structure development in RIM copolymers,” *Polymer*, vol. 36, no. 18, pp. 3555–3564, 1995.

[37] K. Norrman, A. Ghanbari-Siahkali, and N. B. Larsen, “Studies of spin-coated polymer films,” *Annual Reports Section “C” (Physical Chemistry)*, vol. 101, p. 174, 2005.

[38] L. L. Spangler, J. M. Torkelson, and J. S. Royal, “Influence of solvent and molecular weight on thickness and surface topography of spin-coated polymer films,” *Polymer Engineering and Science*, vol. 30, no. 11, pp. 644–653, Jun. 1990.

[39] R. . Synowicki, “Spectroscopic ellipsometry characterization of indium tin oxide film microstructure and optical constants,” *Thin Solid Films*, vol. 313–314, pp. 394–397, Feb. 1998.

[40] J. Hale and B. Johs, “CompleteEASE.” J.A. Woollam Co., Inc, 2011.

[41] C. M. Herzinger, B. Johs, W. A. McGahan, J. A. Woollam, and W. Paulson, “Ellipsometric determination of optical constants for silicon and thermally grown silicon dioxide via a multi-sample, multi-wavelength, multi-angle investigation,” *Journal of Applied Physics*, vol. 83, no. 6, p. 3323, 1998.

[42] A. H. Al-Bayati, K. G. Orrman-Rossiter, J. a. van den Berg, and D. G. Armour, “Composition and structure of the native Si oxide by high depth resolution medium energy ion scattering,” *Surface Science Letters*, vol. 241, no. 1–2, p. A5, Jan. 1991.

[43] I. Hamberg and C. G. Granqvist, “Evaporated Sn-doped In2O3 films: Basic optical properties and applications to energy-efficient windows,” *Journal of Applied Physics*, vol. 60, no. 11, p. R123, 1986.

[44] T. Stoica, M. Gartner, and M. Zaharescu, “Ellipsometric studies of indium tin oxide films deposited by sol-gel process,” in *CAS ’99 Proceedings*, 1999, vol. 1, pp. 381–384.

[45] M. Kanehara, H. Koike, T. Yoshinaga, and T. Teranishi, “Indium tin oxide nanoparticles with compositionally tunable surface plasmon resonance frequencies in the near-IR region.,” *Journal of the American Chemical Society*, vol. 131, no. 49, pp. 17736–7, Dec. 2009.

[46] G. Spathis, M. Niaounakis, E. Kontou, L. Apekis, P. Pissis, and C. Christodoulides, “Morphological changes in segmented polyurethane elastomers by varying the NCO/OH ratio,” *Journal of Applied Polymer Science*, vol. 54, no. 7, pp. 831–842, Nov. 1994.

[47] D. Lee and H. Tsai, “Properties of segmented polyurethanes derived from different diisocyanates,” *Journal of Applied Polymer Science*, vol. 75, no. 1, pp. 167–174, Jan. 2000.

[48] T. A. Speckhard, G. Ver Strate, P. E. Gibson, and S. L. Cooper, “Properties of polyisobutylene-polyurethane block copolymers: I. Macroglycols from ozonolysis of isobutylene-isoprene copolymer,” *Polymer Engineering and Science*, vol. 23, no. 6, pp. 337–349, Apr. 1983.

[49] E. J. Woo, G. Farber, R. J. Farris, C. P. Lillya, and J. C. W. Chienf, “Structure-Property Relationships in Thermoplastic Elastomers: I. Segmented pol yether-Polyurethanes,” no. 13, 2000.

[50] P. J. Yoon and C. D. Han, “Effect of Thermal History on the Rheological Behavior of Thermoplastic Polyurethanes,” *Macromolecules*, vol. 33, no. 6, pp. 2171–2183, Mar. 2000.

[51] E. Kontou, G. Spathis, M. Niaounakis, and V. Kefalas, “Physical and chemical cross-linking effects in polyurethane elastomers,” *Colloid & Polymer Science*, vol. 268, no. 7, pp. 636–644, Jul. 1990.

[52] K. Words, “Thermal Stability of Polyurethanes,” 1988.

[53] F. M. B. Coutinho, M. C. Delpech, T. L. Alves, and A. a. Ferreira, “Degradation profiles of cast films of polyurethane and poly(urethane-urea) aqueous dispersions based on hydroxy-terminated polybutadiene and different diisocyanates,” *Polymer Degradation and Stability*, vol. 81, no. 1, pp. 19–27, Jan. 2003.

[54] P. Wang, W.-Y. Chiu, L. Chen, B. Denq, T. Don, and Y. Chiu, “Thermal degradation behavior and flammability of polyurethanes blended with poly(bispropoxyphosphazene),” *Polymer Degradation and Stability*, vol. 66, no. 3, pp. 307–315, Dec. 1999.

[55] G. Trovati, E. A. Sanches, S. C. Neto, Y. P. Mascarenhas, and G. O. Chierice, “Characterization of polyurethane resins by FTIR, TGA, and XRD,” *Journal of Applied Polymer Science*, vol. 115, no. 1, pp. 263–268, Jan. 2010.

[56] G. Beaucage, R. Composto, and R. S. Stein, “Ellipsometric study of the glass transition and thermal expansion coefficients of thin polymer films,” *Journal of Polymer Science Part B: Polymer Physics*, vol. 31, no. 3, pp. 319–326, Mar. 1993.